

## Article

## Firefly-Inspired Approach to Develop New Chemiluminescence Materials



Yuxing Yan, Shuo Wang, Fuli Xie, Xiaofeng Fang, Yu-Mo Zhang, Sean Xiao-An Zhang

zhangyumo@jlu.edu.cn

**HIGHLIGHTS**

New chemiluminescent materials inspired by bioluminescence have been designed

A way to design new chemiluminescent materials is reported

The relationship of enol-degradation and chemiluminescence is methodically discussed

Yan et al., iScience 13, 478–487  
March 29, 2019 © 2019 The Author(s).  
<https://doi.org/10.1016/j.isci.2019.02.003>

## Article

## Firefly-Inspired Approach to Develop New Chemiluminescence Materials

Yuxing Yan,<sup>1,2,3</sup> Shuo Wang,<sup>1,2,3</sup> Fuli Xie,<sup>1,2</sup> Xiaofeng Fang,<sup>1,2</sup> Yu-Mo Zhang,<sup>1,2,4,\*</sup> and Sean Xiao-An Zhang<sup>1,2</sup>

## SUMMARY

**Bioluminescence, wherein marine and terrestrial organisms chemically produce light for communication, is a burgeoning area of research. Herein, we demonstrate a new series of artificial chemiluminescent compounds inspired by the enol-degradation reaction of natural bioluminescent molecules, luciferins. Based on systematic optical experiments, isotope labeling, and theoretical calculations, the chemiluminescent mechanism of these new materials and the relationship of enol-degradation reaction and chemiluminescence are fully discussed. The color and efficiency of the artificial chemiluminescent materials can be easily adjusted, and blue (486 nm), yellow (565 nm), and near-infrared (756 nm) luminescence can thus be obtained. The findings and in-depth understanding herein may accelerate the development of bio/chemiluminescent materials for analytical applications and non-invasive bioluminescence imaging.**

## INTRODUCTION

Bioluminescence as an amazing phenomenon is well known to most people, and can be found in many living organisms, such as firefly, mollusks, and jellyfishes (Tsarkova et al., 2016). Different species of marine and terrestrial organisms often use various proteins and substrates (Kaskova et al., 2016). Interestingly, many known bioluminescent reactions belong to an enol-degradation (ED) reaction as shown in Scheme 1, such as aldehydes catalyzed by horseradish peroxidase and imidazopyrazinone derivatives catalyzed by luciferase (Yue et al., 2012; Navizet et al., 2011). Specifically, the generally accepted bioluminescence mechanism involves the following steps: (1) the generation of the enolate form catalyzed by luciferase and (2) the emission of visible light through the decomposition of dioxetanone formed by the oxygenation and degradation of the enolate form with O<sub>2</sub> (Scheme 1). Many novel luciferin analogs containing different substitutions with luminescent properties have been designed and successfully applied for the sensitive detection of harmful substances *in vivo* (Takakura et al., 2015; Van de Bittner et al., 2013), and for non-invasive bioluminescence imaging in preclinical cancer research (Kuchimaru et al., 2016; Rehemtulla et al., 2000; Luker et al., 2004; Heffern et al., 2016). Unfortunately, the relationship of ED reaction and luminescence is not entirely clear. It is still unclear why some ED reactions can emit light, whereas the others cannot and why most biomimetic chemiluminescent efforts via specially designed enol-degradable molecules have failed (Zhang et al., 2014, 2017). Therefore, a great perplexity hereon is what actually are the key factors of ED reactions to re-transform chemical energy to light.

Chemiluminescent materials, similar to bioluminescent materials without external light excitation, offer many obvious advantages over fluorescence materials based on photon emission, such as high signal-to-noise ratio and significantly reduced photodamage and photobleaching (Moddord et al., 2014; Jones et al., 2017). Thus chemiluminescence is a well-established technology applied to many areas of biological analysis. However, limited diversity restricts the development of the chemiluminescence. One important method to develop a new class of chemiluminescent materials is the simulation of bioluminescent ED reactions. For example, enol forms of acridinium esters oxidized by hydrogen peroxide have been used in analytical applications (Natrajan et al., 2014). Herein, we present a novel series of artificial chemiluminescent materials inspired by the amazing ED reaction of natural bioluminescent molecules. Eighteen molecules have been studied, and the structural features and essential influencing factors of the ED reactions to achieve chemiluminescence have been discussed in depth by contrasting ED with light emission and ED without light emission.

## RESULTS

## Chemiluminescence

For an in-depth study of the relationship of ED reactions and luminescence, 18 molecules containing structural feature of  $\alpha$ -H with different leaving groups and rigid structures were synthesized and prepared in

<sup>1</sup>State Key Laboratory of Supramolecular Structure and Materials, College of Chemistry, Jilin University, Changchun, Jilin 130012, China

<sup>2</sup>College of Chemistry, Jilin University, Changchun, Jilin 130012, China

<sup>3</sup>These authors contributed equally

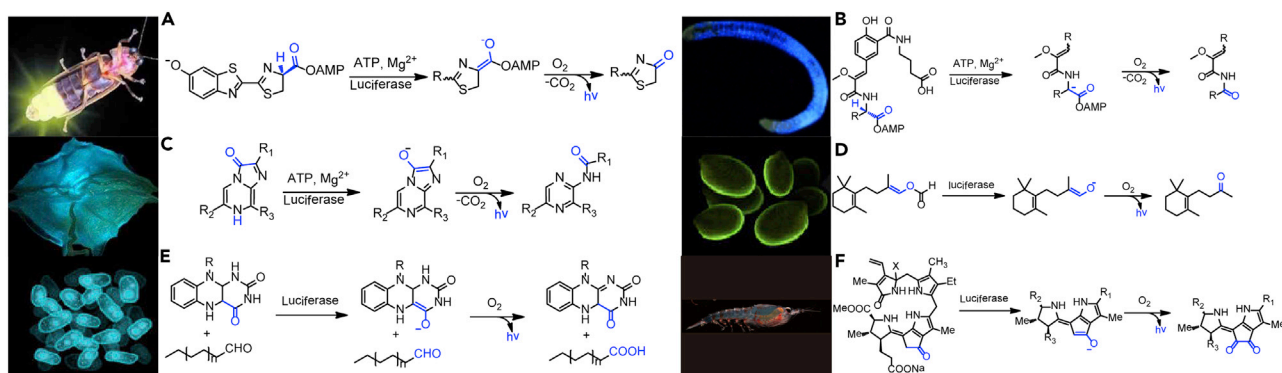
<sup>4</sup>Lead Contact

\*Correspondence:

zhangyumo@jlu.edu.cn

<https://doi.org/10.1016/j.isci.2019.02.003>





**Scheme 1. Substrates and Mechanisms of Known Bioluminescence Reactions (A) Firefly luciferin (B) *Fridericia heliota* luciferin (C) *Cypridina* luciferin (D) *Latia* luciferin (E) *Bacteria* luciferin (F) *Euphausiid* luciferin.**

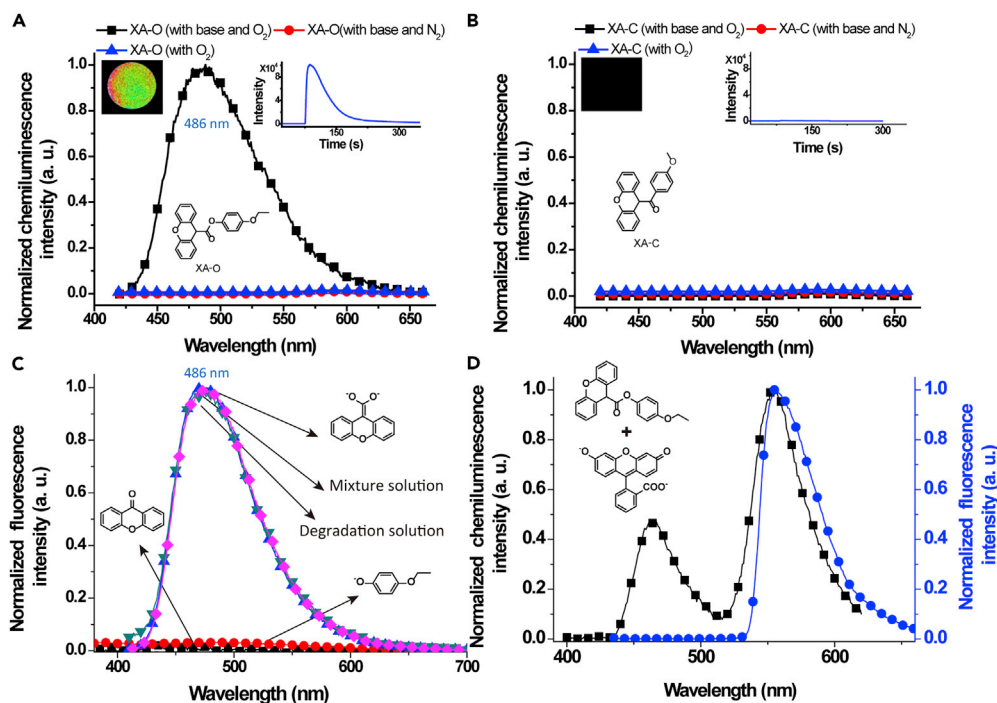
**Supplemental Information.** For this, **XA-O** and **XA-C** synthesized by a rigid xanthoic acid with phenol (**XA-O**) or phenyl (**XA-C**) were first chosen as examples. The enzyme's function of proton extraction was imitated by chemical base to simplify the bioluminescent model that was used before by eminent researchers for studying the bioluminescence mechanism (White et al., 1980; Nakatani et al., 2007; Vacher et al., 2018; Freeman et al., 2011). To our great surprise, bright blue-white light at 486 nm was observed in **XA-O** solution stimulated by base (potassium tert-butoxide [KTB]) under an oxygen atmosphere in Figure 1A. After adding base under an oxygen atmosphere, the luminescence intensity increased rapidly to a peak value and then decreased to zero, as shown in the chemiluminescent kinetic curve of Figure 1A. However, no light emission can be detected by base or oxygen alone. The degradation process was investigated by absorption spectroscopy (Figure S1). After adding the base, new absorption peaks at 376 and 312 nm were instantly observed corresponding to the enolate form of **XA-O**, indicating that the deprotonation of **XA-O** was the first degradation step. Then after exposure to oxygen, the intensity of both peaks 312 and 376 nm were decreased over time and disappeared finally, along with the appearance of new peaks at 337, 326, and 279 nm assigned as the characteristic peaks of the degradation products of **XA-O**.

**XA-C**, which possessed a similar structure as **XA-O**, did not exhibit any chemiluminescent properties (Figure 1B). Interestingly, **XA-C** underwent similar degradation process after stimulation with base and oxygen as shown in Figure S2. The enolate form of **XA-C** with characteristic peaks at 374 and 300 nm was generated first after adding base in nitrogen atmosphere, and then new peaks characteristic of degradation products appeared after being exposed to oxygen. Such differences inspired us to explore the detailed relationship of the ED reaction and luminescence and to deeply understand the key factors of ED reactions for luminescence.

### The Chemiluminescence Mechanism

To understand the ED mechanism, three observable degradation products of **XA-O**, containing xanthone, o-ethoxyphenol, and xanthoic acid, were carefully isolated by column chromatography, which were confirmed further by nuclear magnetic resonance (NMR) (Figure S3). These results were also supported by the absorption peaks of the degradation solution, comparing the characteristic peaks of xanthone, o-ethoxyphenol, and xanthoic acid in Figure S1.

The mass spectrum (MS) of the ED solution of **XA-O** under an  $^{18}\text{O}_2$  atmosphere without further post-treatment was measured then. In Figure 2A (positive mode) and Figure S4 (negative mode), the major peak at 199.07 was assigned to xanthone  $[(M+2)+\text{H}]^+$ . Also, other peaks at 139.13, 227.07, and 181.07 were identical to the theoretical molecular weights of o-ethoxyphenol  $[M + \text{H}]^+$  and xanthoic acid  $[M + \text{H}]^+ [M-\text{CO}_2]^+$  compared with the MS of xanthoic acid in Figure S4. The appearance of  $[^{18}\text{O}]$ -labeled xanthone suggested that the enolate of **XA-O** was oxidized by the addition of two oxygen atoms and then decomposed to xanthone. Considering  $[^{18}\text{O}]$ -labeled xanthone and  $[^{16}\text{O}]$ -labeled o-ethoxyphenol as degradation products, the mass difference of 12 amu indicated the loss of a single carbon atom, which agreed with the reactions of  $\text{O}_2$  addition and  $\text{CO}_2$  release. Carbon dioxide elimination was a dominant dissociation pathway in ED (i.e., for luciferin). Therefore the ED mechanism of **XA-O** was proposed as shown in Figure 2C. First, the four-ring structure (Int 2) of **XA-O** was formed by the oxygenation of the



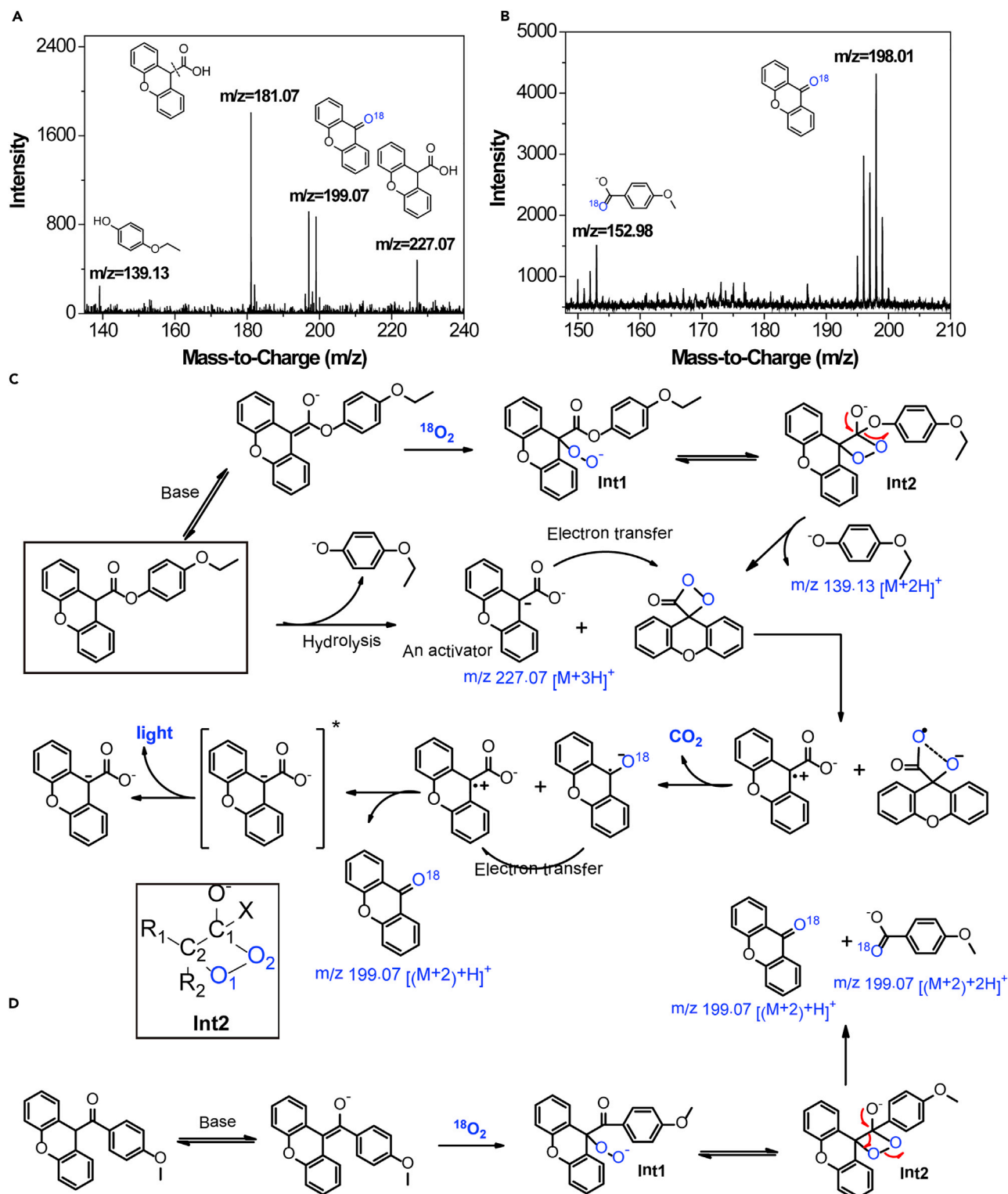
**Figure 1. Chemiluminescent Properties of XA-O and XA-C**

(A and B) Chemiluminescent spectra of (A) XA-O and (B) XA-C stimulated by KTB under oxygen (black curve), KTB alone (red curve), and oxygen alone (blue curve) in dimethylformamide (DMF). Inset: chemiluminescence kinetics and images. (C) Photoluminescence spectra of xanthone, *o*-ethoxyphenol, xanthic acid, the mixture of the three compounds, and the degradation mixture in the presence of 20 equiv. KTB and oxygen in DMF. (D) Chemiluminescent spectrum (black curve) of a mixture of XA-O and fluorescein, and photoluminescence spectrum (blue curve) of fluorescein in DMF in the presence of KTB.

enolate form generated by the surrounding base. Then, Int 2 was decomposed into dioxetanone as a high-energy intermediate and 4-ethoxyphenolate. Finally, carbon dioxide, xanthone, and light were produced by the decomposition of dioxetanone. The decomposition mechanism of dioxetanone is discussed below.

Owing to the generation of xanthic acid, we can infer that the hydrolysis of XA-O occurred. Next, the hydrolysis of XA-O was observed to confirm the relationship between hydrolysis and chemiluminescence. XA-O hydrolyzed completely after the addition of a base in a methanol-water solution under oxygen atmosphere. However, light cannot be detected during the reference reactions, as shown in the chemiluminescent kinetic curves and image in Figure S5. This result indicated clearly that the hydrolysis of XA-O was a side reaction for the emission of light.

Surprisingly, we discovered that the chemiluminescence spectrum of XA-O was the same as the photoluminescence spectrum of dual-ionized xanthic acid (486 nm, the form of xanthic acid under 20 equiv. KTB, which was undoubtedly proven by its fluorescence and NMR spectra in Figure S6), instead of that of xanthone in Figure 1C (the emission peak of xanthone was at 425 nm without base, and fluorescence quantum yield [QY] is zero under 20 equiv. KTB in Figure S6). These strongly supported that the decomposition mechanism of dioxetanone was intermolecular chemically initiated electron exchange, not unimolecular decomposition based on many excellent articles about decomposition of 1,2-dioxetanones (Vacher et al., 2018; Augusto et al., 2013; Stevani et al., 2000). Thus, we proposed the decomposition mechanism of dioxetanone as shown in Figure 2. The 1,2-dioxetanone was decomposed into carbon dioxide and the xanthone radical anion catalyzed by electron transfer from the xanthic acid dianion as an activator. Then, the excited singlet state of xanthic acid was generated through electron backtransfer from the xanthone radical anion. This mechanism was further confirmed by the mixture of fluorescein (as an activator) in Figure 1D. A delightful fluorescence of fluorescein was detected when it was mixed into the XA-O



**Figure 2. Mechanisms of ED Reactions**

(A–D) MS of (A) XA-O (positive MS) and (B) XA-C (negative MS) stimulated by KTB under an  $^{18}\text{O}_2$  atmosphere without further post-treatment. Proposed mechanisms for the ED of (C) XA-O and (D) XA-C.



solution. At the same time, light cannot be detected when hydrolysis reaction of **XA-O** was avoided in anhydrous dimethylformamide (DMF) (Transparent Methods); nevertheless, light can appear when mixing fluorescein in anhydrous DMF (Figure S7).

The ED products (xanthone and *p*-anisic acid) of **XA-C** without chemiluminescent properties were isolated by column chromatography and confirmed by NMR spectroscopy in Figure S8. Then, MS of the ED solution under an  $^{18}\text{O}_2$  atmosphere without further post-treatment was also obtained. As shown in Figure 2B (negative mode) and Figure S4 (positive mode), two major peaks at 198.01 and 152.98 were assigned to xanthone  $[\text{M}+2]^+$  and *p*-anisic acid  $[(\text{M}+2)-\text{H}]^+$ . The appearance of  $^{18}\text{O}$ -labeled xanthone and *p*-anisic acid indicated that the enolate of **XA-C** was also oxidized by the addition of two oxygen atoms and then decomposed to form xanthone and *p*-anisic acid. Therefore the degradation mechanism of **XA-C** was proposed (Figure 2D). First, the enolate form was generated under basic conditions. Then, oxygen was captured to form an Int 2, which was immediately decomposed to a carboxylic acid and ketone.

In the two ED mechanisms, Int 2 formed by the addition of two oxygen atoms was a common high-energy unstable intermediate. However, the decomposition path was considerably different. For chemiluminescent **XA-O**, dioxetanone was formed in ED reaction, and the C-O bond linking the carbonyl and leaving group (phenol) was broken. For non-chemiluminescent **XA-C**, there was no dioxetanone intermediate, and the C-C bond linking the carbonyl and  $\alpha$ -C was broken. That means, we can propose that the formation of dioxetanone and the cleavage energies of these two bonds were crucial to understand the degradation path and chemiluminescent properties.

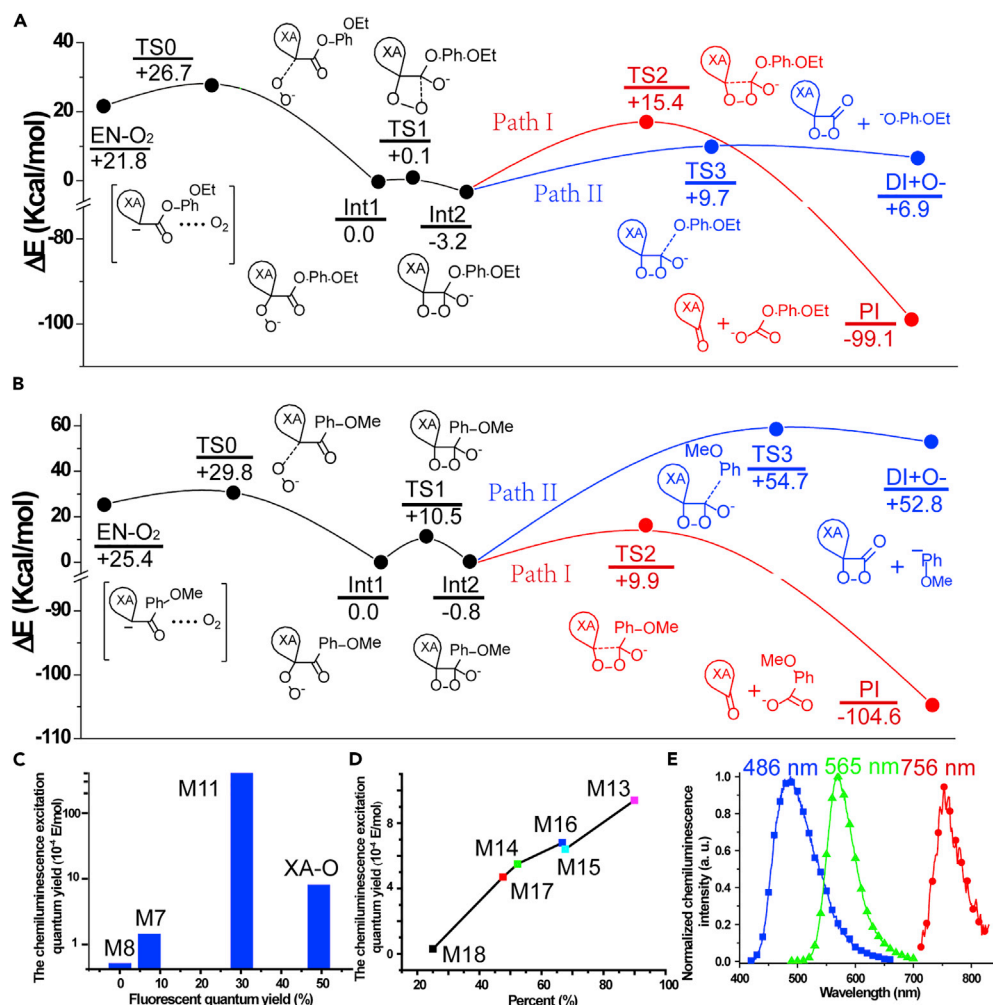
In addition, femtosecond transient absorption spectroscopy (FTAS) was attempted to verify the formation of dioxetanone, which was a very difficult issue in research of bio/chemiluminescence mechanism (Usami and Isobe, 1996). **M11** and **M12** as reference molecules containing 400-nm absorbances were synthesized and detected by FTAS (Figures S9 and S10), owing to the limit of the 400-nm excitation light source. Fortunately, a new peak at 511 nm was detected only in the ED process of **M11**, compared with the spectra of the ED process of **M12**. Maybe, the 511-nm peak was an evidence to support the identity of the dioxetanone.

### Density Functional Theory Analysis

To further understand the relationship of the ED pathway and the reactant structures, the potential energy surfaces of the ED reactions for **XA-O** and **XA-C** were analyzed by UCAM-B3LYP/6-31G(d,p) (Frisch et al., 2009). As shown in Figure 3, **XA-C** and **XA-O** both had two possible pathways (I and II) and three energy barriers, including molecular oxygen capture and the formation and decomposition of Int 2.

The oxygen molecule (triplet) first attacked the enolate form of **XA-O** to form a C2-O1 bond and peroxide anion (Int 1) through a single electron transfer mechanism (Liu et al., 2009), which is discussed in detail in Figure S11. Then new C1-O2 bond and four-membered ring (Int 2) were formed by overcoming a small barrier of 0.1 kcal/mol. Two possible reaction pathways were studied for the decomposition of Int 2. In path I, the C1-C2 bond was stretched and 18.6 kcal/mol energy had to be overcome to generate xanthone and the carbonate compound (P1). However,  $^{18}\text{O}$ -labeled P1 ( $[\text{M}+2]$ : 184.06) cannot be detected by MS (Figure 2A). In path II, only 12.9 kcal/mol energy was needed, and the C1-X (C1-O) bond was first stretched. Thus path II was preferred based on the thermomechanical analysis. The highest energy barrier was only 12.9 kcal/mol in the entire potential energy curve of ED of **XA-O**, which meant that this process was a spontaneous thermodynamic reaction.

The potential energy curves of the ED process of **XA-C** is shown in Figure 3B. **XA-C** and **XA-O** had similar potential energy curves before the decomposition of Int 2. The difference was the decomposition path of Int 2. By analyzing the decomposition pathway of Int 2, path I was preferred based on thermomechanical analysis, which was consistent with our experimental results. Compared with potential energy curves of **XA-C** and **XA-O**, the degradation pathway was dependent on the breakage energy difference of the C-C (C1-C2 for **XA-O** and **XA-C** linking the carbonyl and  $\alpha$ -C) and C-X bonds (C1-O for **XA-O** and C1-C for **XA-C** linking the carbonyl and leaving group). In path I, the decomposition of C-C was easier than that of the C-X bond. However, C-X was preferentially decomposed over the C-C bond to form dioxetanone in path II. Thus the formation of the dioxetanone for ED reaction required the C-X bond to be preferentially cleaved and depended on the leaving group. This means, we can predict the chemiluminescent



**Figure 3. Potential Energy Surfaces of XA-O and XA-C and Chemiluminescent Properties of M3-M18**

(A and B) Potential energy surfaces of the generation and degradation taking different pathways for (A) XA-O and (B) XA-C computed at the UCAM-B3LYP/6-31G(d,p) level.

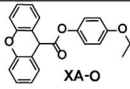
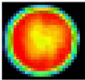
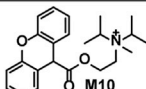
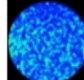
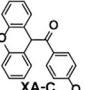

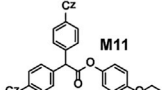
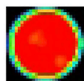
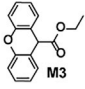

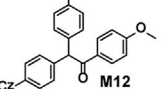

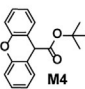

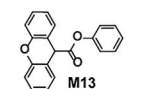
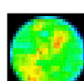
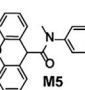

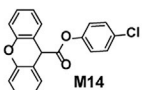
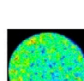
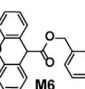

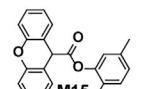
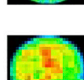
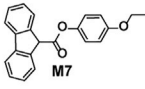
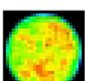
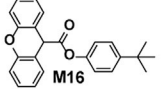
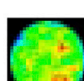
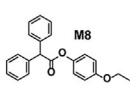

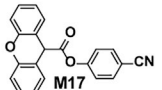
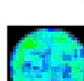
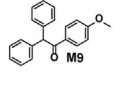

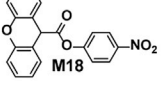
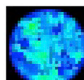
(C) Dependency of chemiluminescence excitation quantum yield on the QY of the activator.

(D) Dependency of chemiluminescence excitation quantum yield on the ED percent.

(E) Chemiluminescent spectra of **M8** solution mixed with xanthoic acid (blue curve), fluorescein (green curve), and 2-(2-(4-hydroxystyryl)-4H-chromen-4-ylidene)malononitrile (red curve).

property of the ED reaction and the formation of dioxetanone by comparing the energies of TS2 of path I and TS3 of path II.

To further verify this inference, optical properties and bond cleavage energy barriers of 16 other molecules with different leaving groups were also studied in Table 1. Compared with **M3**, **M4**, **M6**, and **M10** containing the same C-O linking group between the carbonyl and the different leaving groups, chemiluminescence can be observed only if the energy of TS3 was smaller than that of TS2. This means that the chemiluminescent property was not dependent on the kind of linking bond. We also found that the bond cleavage energy barrier can be affected by the electron-withdrawing ability of the leaving group. For example, the energy of TS2 of **M3** with ethyl group as leaving group was 10.7 kcal/mol, which was smaller than that of TS3 (54.9 kcal/mol). However, **M10** with ethyl group substituted by quaternary ammonium salt exhibited contrary result. The energies of TS2 and TS3 were 17.2 kcal/mol and 14.8 kcal/mol, respectively. Therefore, Int 2 of **M10** preferentially underwent C-O bond cleavage over C-C bond cleavage, indicating that **M10** would exhibit chemiluminescence consistent with our experimental results observed

Compound	TS2 <=> TS3 (kcal/mol) Pathway	CL image	$\lambda_{em}$ (nm)	$\Phi_{CL}(10^{-4})$ / $\Phi_s(10^{-3})$ [E mol <sup>-1</sup> ]	Compound	TS2 <=> TS3 (kcal/mol) Pathway	CL image	$\lambda_{em}$ (nm)	$\Phi_{CL}(10^{-4})$ / $\Phi_s(10^{-3})$ [E mol <sup>-1</sup> ]
	18.6 > 12.9 (II)		486	7.8/1.6		17.2 > 14.8 (II)		486	0.37/0.67
	10.7 < 54.9 (I)		--	--		16.8 > 13.9 (II)		506	390/129
	19.2 < 31.3 (I)		--	--		10.2 < 57.7 (I)		--	--
	17.4 < 24.4 (I)		--	--		19.7 > 11.5 (II)		486	9.4/1.9
	11.8 < 21.5 (I)		--	--		24.2 > 9.4 (II)		486	5.5/1.1
	16.8 < 27.3 (I)		--	--		20.4 > 11.9 (II)		486	6.4/1.4
	12.6 > 11.1 (II)		550	1.4/5.0		19.3 > 12.1 (II)		486	6.8/1.4
	12.9 > 10.3 (II)		--	--		25.4 > 1.0 (II)		486	4.7/0.78
	12.8 < 55.2 (I)		--	--		25.9 > 2.0 (II)		486	0.3/0.06

**Table 1. The Structures, Calculated Energy Barriers (Kcal/mol) of Decomposition of Int 2 in Path I (TS2) and II (TS3), Pathway Predicted by DFT, Chemiluminescent (CL) Images, the Maximum Wavelength of Chemiluminescence ( $\lambda_{em}$ ), the Chemiluminescence ( $\Phi_{CL}$ ), and Singlet ( $\Phi_s$ ) Excitation Quantum Yield of XA-O, XA-C, and M3–M18**

by the chemiluminescent image in Table 1. Other molecules also followed the rule that TS2 was smaller than TS3 for chemiluminescence. For example, the energy of TS2 of amide-linked M5 was 11.8 kcal/mol and that of TS3 was 21.5 kcal/mol, as shown in the potential energy curves of M5 (Figure S12). Therefore Int 2 of M5 preferentially underwent C-C bond cleavage over C-N bond cleavage, and the ED of M5 would occur through path I, similar to XA-C. This calculation result indicated that the dioxetanone was not formed and M5 did not exhibit chemiluminescence, which was consistent with our experimental results (Table 1). All the molecules proved that the formation of the dioxetanone and chemiluminescence required that the C-X linking the carbonyl and the different leaving group was more prone to breakage.

### Chemiluminescent Intensity and Color

Based on the chemiluminescence mechanism of the new compounds, we can speculate that the chemiluminescent intensity of the ED reaction depended on the fluorescence QY of the activator, the percent of



enolate form, and ED reaction. Regarding this, the pKa of  $\alpha$ -H was key for the amount of enolate form, and the relationship of pKa and enol-ketone equilibrium reaction had been thoroughly discussed by many excellent works (Sloop et al., 2006; Jimenez-Cruz et al., 2015; Belova et al., 2010). In this work, to study exactly the relationship of ED reaction and chemiluminescence, and to avoid the interference of enol-ketone equilibrium reaction, excess base (20 equiv. t-BuOK) in our experiments was used to confirm that the enol-ketone equilibrium reaction was not the rate-determining step for ED reaction and ketone form had been transferred into enolate form completely.

The chemiluminescence and the singlet excitation QYs of the chemiluminescent compounds were measured using the luminol standard for photomultiplier calibration (Augusto et al., 2013; Stevani et al., 2000). As shown in Table 1, the new compounds exhibited the desirable intensity (Augusto et al., 2013). Compared with M8, M7, and M11 containing the same leaving group and different acid as activator, the chemiluminescence and the singlet excitation QYs were proportional to the QY of activator in Figure 3C. QY of dual-ionized form of 2,2-bis(4-(9H-carbazol-9-yl)phenyl)acetic acid as the activator for M11 was 30.2%, which was more than four times that of 9H-fluoren-9-one (7.3%) as the activator for M7; also, the chemiluminescence and the singlet excitation QYs of M11 ( $3.9 \times 10^{-2}/1.29 \times 10^{-1}$  E/mol) were hundreds of times larger than those of M7 ( $1.4 \times 10^{-4}/5.0 \times 10^{-3}$  E/mol). M8 did not exhibit chemiluminescent property, and therefore its QY was zero, although the formation of the dioxetanone was verified to be predicted by DFT method in Table 1. In addition, QY of dual-ionized xanthoic acid was about 50%, but its chemiluminescence and singlet excitation QY ( $7.8 \times 10^{-4}/1.6 \times 10^{-3}$  E/mol) was smaller than that of M11, which indicated that the chemiluminescent intensity was affected by multiple factors.

Hydrolysis, as a competing reaction for ED reaction, was also a factor for the chemiluminescent intensity. Molecules containing the same leaving group with different substituents were designed to study the influence of hydrolysis, labeled as M13–M18 in Table 1. M18 containing nitro as electron-withdrawing substituent exhibited high percentage of hydrolysis, about 75%, and low percentage of degradation, about 25%. Also, its chemiluminescence and singlet excitation QY was about  $7.8 \times 10^{-4}$  E/mol and  $1.6 \times 10^{-3}$  E/mol, respectively. The chemiluminescence and singlet excitation QY can increase more than 30 times by removing the electron-withdrawing substituent, such as M13. As shown in Figure 3D, the chemiluminescence and singlet excitation QYs were proportional to the percent of ED reaction regulated by the electron-donating ability of substituent, and were inversely proportional to hydrolysis percent.

Based on the abovementioned discussion, we can confirm that the chemiluminescent intensity of these new compounds exhibited plenty of room by optimizing the electron-donating ability of substituents to regulate the ED percent and optimizing QY of acid as the activator. The chemiluminescent color depended on the color of the activator in the ED reaction. As shown in Figure 3E, the color was blue (486 nm) when xanthoic acid was mixed into the ED solution of M8, which cannot emit light alone. Meanwhile, the color was turned to yellow (565 nm) or red (756 nm) when fluorescein or (E)-2-(2-(4-hydroxystyryl)-4H-chromen-4-ylidene) malononitrile, respectively, was mixed. Thus the color can be fine-tuned by mixing fluorescent materials with different colors.

## DISCUSSION

In this study, the relationship of ED and luminescence was systematically confirmed for the first time. Two important factors for bio/chemiluminescence via ED are clearly demonstrated: the formation of dioxetanone intermediates, which is dependent on the leaving group, and the QY of the activator. The luminescence intensity and color rests with the QY and color of the activator. These findings demonstrate a new way to fabricate new luminescent materials. We believe that this work not only will accelerate research to deeply understand the mechanism and evolution of bioluminescence but also will open new methods to synthesize new chemiluminescent materials to develop novel artificial light systems, analytical tools, and non-invasive bioluminescence imaging.

### Limitations of the Study

To verify the relationship of ED and chemiluminescence and to design new chemiluminescent materials inspired by ED of bioluminescence, we used isotope labeling method and theoretical calculations to discuss systematically the ED mechanism. However, dioxetanone as the intermediate was not captured by NMR or MS. Therefore it is necessary to use new characterization methods to investigate the mechanism in further work.

## METHODS

All methods can be found in the accompanying Transparent Methods supplemental file.

## SUPPLEMENTAL INFORMATION

Supplemental Information includes Transparent Methods, 46 figures, and 1 data file and can be found with this article online at <https://doi.org/10.1016/j.isci.2019.02.003>.

## ACKNOWLEDGMENTS

This work was financially supported by the National Natural Science Foundation of China (Grant No. 21602075), by Natural Science Foundation of Jilin Province (CN) (No. 20180520155JH), and by Young Elite Scientist Sponsorship Program by Jilin Province (CN) (181903).

## AUTHOR CONTRIBUTIONS

Y.Y., S.W., X.F., and F.X. performed all the experiments; Y.Y., S.W., and Y.-M.Z. analyzed the experimental data; Y.-M.Z. conducted the theoretical computations and analyzed the data; and Y.M. Z. and S. X.-A.Z. reviewed and co-wrote the manuscript.

## DECLARATION OF INTERESTS

Authors declare no conflict of interest.

Received: August 18, 2018

Revised: November 26, 2018

Accepted: February 4, 2019

Published: March 14, 2019

## REFERENCES

- Augusto, F.A., de Souza, G.A., de Souza Junior, S.P., Khalid, M., and Baader, W.J. (2013). Efficiency of electron transfer initiated chemiluminescence. *Photochem. Photobiol.* *89*, 1299–1317.
- Belova, N.V., Sliznev, V.V., Oberhammer, H., and Girichev, G.V. (2010). Tautomeric and conformational properties of  $\beta$ -diketones. *J. Mol. Struct.* *978*, 282–293.
- Van de Bittner, G.C., Bertozzi, C.R., and Chang, C.J. (2013). Strategy for dual-analyte luciferin imaging: *in vivo* bioluminescence detection of hydrogen peroxide and caspase activity in a murine model of acute inflammation. *J. Am. Chem. Soc.* *135*, 1783–1795.
- Freeman, R., Liu, X., and Willner, I. (2011). Chemiluminescent and chemiluminescence resonance energy transfer (CRET) detection of DNA, metal ions, and aptamer–substrate complexes using hemin/G-quadruplexes and CdSe/ZnS quantum dots. *J. Am. Chem. Soc.* *133*, 11597–11604.
- Frisch, M.J., Schlegel, H.B., Scuseria, G.E., Robb, M.A., Cheeseman, J.R., Scalmani, G., Barone, V., Mennucci, B., Petersson, G.A., Nakatsuji, H., et al. (2009). GAUSSIAN 09 (Gaussian Inc.).
- Heffern, M.C., Park, H.M., Au-Yeung, H.Y., Van de Bittner, G.C., Ackerman, C.M., Stahl, A., and Chang, C.J. (2016). *In vivo* bioluminescence imaging reveals copper deficiency in a murine model of nonalcoholic fatty liver disease. *Proc. Natl. Acad. Sci. U S A* *113*, 14219–14224.
- Jimenez-Cruz, F., Ríos-Olivares, H., García-Gutierrez, J.L., and Fragoza Mar, L. (2015). Electronic effects on keto-enol tautomerism of *p*-substituted aryl-1,3-diketone malonates. *J. Mol. Struct.* *1101*, 162–169.
- Jones, K.A., Porterfield, W.B., Rathbun, C.M., McCutcheon, D.C., Paley, M.A., and Prescher, J.A. (2017). Orthogonal luciferase-luciferin pairs for bioluminescence imaging. *J. Am. Chem. Soc.* *139*, 2351–2358.
- Kaskova, Z.M., Tsarkova, A.S., and Yampolsky, I.V. (2016). 1001 lights: luciferins, luciferases, their mechanisms of action and applications in chemical analysis, biology and medicine. *Chem. Soc. Rev.* *45*, 6048–6077.
- Kuchimaru, T., Lwano, S., Kiyama, M., Mitsumata, S., Kadosono, T., Niwa, H., Maki, S., and Kizaka-Kondoh, S.A. (2016). A luciferin analogue generating near-infrared bioluminescence achieves highly sensitive deep-tissue imaging. *Nat. Commun.* *7*, 11856.
- Liu, F., Liu, Y., De Vico, L., and Lindh, R. (2009). Theoretical study of the chemiluminescent decomposition of dioxetanone. *J. Am. Chem. Soc.* *131*, 6181–6188.
- Luker, K.E., Smith, M.C.P., Luker, G.D., Gammon, S.T., Piwnica-Worms, H., and Piwnica-Worms, D. (2004). Kinetics of regulated protein-protein interactions revealed with firefly luciferase complementation imaging in cells and living animals. *Proc. Natl. Acad. Sci. U S A* *101*, 12288–12293.
- Moddord, D.M., Reddy, G.R., and Miller, S.C. (2014). Latent luciferase activity in the fruit fly revealed by a synthetic luciferin. *Proc. Natl. Acad. Sci. U S A* *111*, 4443–4448.
- Nakatani, N., Hasegawa, J.Y., and Nakatsuji, H. (2007). Red light in chemiluminescence and yellow-green light in bioluminescence: color-tuning mechanism of firefly, *Photinus pyralis*, studied by the symmetry-adapted cluster-configuration interaction method. *J. Am. Chem. Soc.* *129*, 8756–8765.
- Natrajan, A., Wen, D., and Sharpe, D. (2014). Synthesis and properties of chemiluminescent acridinium ester labels with fluorine tags. *Org. Biomol. Chem.* *12*, 3887–3901.
- Navizet, I., Liu, Y.J., Ferre, N., Raca-Sanjuan, D., and Lindh, R. (2011). The chemistry of bioluminescence: an analysis of chemical functionalities. *ChemPhysChem* *12*, 3064–3076.
- Rehmetulla, A., Stegman, L.D., Cardozo, S.J., Gupta, S., Hall, D.E., Contag, C.H., and Ross, B.D. (2000). Rapid and quantitative assessment of cancer treatment response using *in vivo* bioluminescence imaging. *Neoplasia* *2*, 491–495.
- Sloop, J.C., Bumgardner, C.L., Washington, G., Loehle, W.D., Sankar, S.S., and Lewis, A.B. (2006). Keto-enol and enol-enol tautomerism in trifluoromethyl- $\beta$ -diketones. *J. Fluor. Chem.* *127*, 780–786.
- Stevani, C.V., Silva, S.M., and Baader, W.J. (2000). Studies on the mechanism of the excitation step in peroxyoxalate system. *Eur. J. Org. Chem.* *24*, 4037–4046.

Takakura, H., Kojima, R., Kamiya, M., Kobayashi, E., Komatsu, T., Ueno, T., Teraï, T., Hanaoka, K., Nagano, T., and Urano, Y. (2015). New class of bioluminogenic probe based on bioluminescent enzyme-induced electron transfer: BioLeT. *J. Am. Chem. Soc.* *137*, 4010–4013.

Tsarkova, A.S., Kaskova, Z.M., and Yampolsky, I.V. (2016). A tale of two luciferins: fungal and earthworm new bioluminescent systems. *Acc. Chem. Res.* *49*, 2372–2380.

Usami, K., and Isobe, M. (1996). Low-temperature photooxygenation of coelenterate luciferin analog synthesis and proof of 1,2-dioxetanone as

luminescence intermediate. *Tetrahedron* *52*, 12061–12090.

Vacher, M., Galván, I.F., Ding, B.-W., Schramm, S., Berraud-Pache, R., Naumov, P., Ferré, N., Liu, Y.J., Navizet, I., Roca-Sanjuán, D., et al. (2018). Chemi- and bioluminescence of cyclic peroxides. *Chem. Rev.* *118*, 6927–6974.

White, E.H., Steinmetz, M.G., Miano, J.D., Wildes, P.D., and Morland, R. (1980). Chemi- and bioluminescence of firefly luciferin. *J. Am. Chem. Soc.* *102*, 3199–3208.

Yue, L., Liu, Y.J., and Fang, W.H. (2012). Mechanistic insight into the chemiluminescent decomposition of firefly dioxetanone. *J. Am. Chem. Soc.* *134*, 11632–11639.

Zhang, Y.M., Wang, X., Li, W., Zhang, W., Li, M., and Zhang, S.X.A. (2014). Bio-inspired enol-degradation for multipurpose oxygen sensing. *Chem. Commun. (Camb)* *50*, 13477–13480.

Zhang, Y.M., Zhang, J., and Zhang, S.X.A. (2017). Luciferin inspired oxygen sensing with alternant change of color and fluorescence. *Dyes Pigm.* *138*, 1–6.

**ISCI, Volume 13**

**Supplemental Information**

**Firefly-Inspired Approach to Develop**

**New Chemiluminescence Materials**

**Yuxing Yan, Shuo Wang, Fuli Xie, Xiaofeng Fang, Yu-Mo Zhang, and Sean Xiao-An Zhang**

## Supplemental Information

### Firefly inspired approach to develop new chemiluminescence materials

Yuxing Yan<sup>a,b,†</sup>, Shuo Wang<sup>a,b,†</sup>, Fuli Xie<sup>a,b</sup>, Xiaofeng Fang<sup>a,b</sup>, Yu-Mo Zhang<sup>a,b\*</sup>, Sean Xiao-An Zhang<sup>a,b</sup>

*a. State Key Laboratory of Supramolecular Structure and Materials, College of Chemistry, Jilin University, Changchun, Jilin 130012, China.*

*b. College of Chemistry, Jilin University, Changchun, Jilin 130012, China.*



## Transparent Methods

### Materials:

Xanthene-9-carboxylic acid (98%), 2-Chloro-1-methylpyridinium iodide (98%), Carbazole (97%), Bis(4-fluorophenyl)-methanone (99%), Sodium borohydride (99%), POCl<sub>3</sub> (99.5%), AlCl<sub>3</sub> (99%), Anisole (99%), Diphenylacetic acid (98%), 2-Hydroxyacetophenone (98%), 4-Ethoxyphenol (98%), N-Methylaniline (98%), tert-Butyllithium, Potassium tert-butanolate (99.9%), 4-Nitrophenol (99%), 4-Cyanophenol, Benzyl alcohol (98%), 9-Carboxyfluorene (98%), 4-chlorophenol (98%), 2,5-Dimethylphenol (98%), Propantheline Bromide (97%), DMF, DMF (spectrum pure), Sodium methanolate were purchased from Energy Chemical. p-Hydroxybenzaldehyde (CP) was purchased from Sinopharm Chemical Reagent. Malononitrile (98%), Sodium hydride, Fluorescein (98%) were purchased from Aladdin. <sup>18</sup>O<sub>2</sub> (97%) was purchased from Shanghai wusheng Biological Technology Co.,Ltd.. Other chemicals were used as received without further purification.

### Methods:

#### Chemiluminescent spectra:

The general procedure of XA-O, XA-C, and M3-M18 for measuring chemiluminescent spectra using XA-O as a template is as follows: 0.5 ml DMF of XA-O ( $1.0 \times 10^{-3}$  M) was injected into quartz cell containing 1 ml DMF solution with potassium t-butoxide ( $1.0 \times 10^{-2}$  M) under oxygen atmosphere monitored by fluorescence spectroscopy.

Control experiment without water: 0.5 ml freshly prepared anhydrous DMF of XA-O ( $1.0 \times 10^{-3}$  M, prepared in a glove box) was injected into quartz cell containing 1 ml freshly prepared anhydrous DMF solution with potassium t-butoxide ( $1.0 \times 10^{-2}$  M, prepared in a glove box) under nitrogen atmosphere, then, oxygen was injected into quartz cell and monitored by a fluorescence spectroscopy.

Hydrolysis: 0.5 ml methanol/DMF (8:2) mixture solution of XA-O ( $1.0 \times 10^{-3}$  M) was injected into quartz cell containing 1 ml methanol/water (8:2) mixture solution with sodium methoxide ( $1.0 \times 10^{-2}$  M) under oxygen atmosphere, and monitored by a fluorescence spectroscopy.

#### Chemiluminescent kinetic curve:

The general procedure of XA-O, XA-C, and M3-M18 for measuring chemiluminescent kinetic

curve using XA-O as a template is as follows: 0.5 ml DMF of XA-O ( $1.0 \times 10^{-4}$  M) was injected into quartz cell containing 1 ml DMF solution with potassium t-butoxide ( $1.0 \times 10^{-3}$  M) under oxygen atmosphere, and monitored by a ultra-weak chemiluminescent analyzer.

### **Chemiluminescent image:**

The general procedure of XA-O, XA-C, and M3-M18 for measuring Chemiluminescent image using XA-O as a template is as follows: 0.1 ml DMF of XA-O ( $1.0 \times 10^{-3}$  M) was injected into cell culture plate (96 cell) containing 0.1 ml DMF solution with potassium t-butoxide ( $2.0 \times 10^{-2}$  M) under oxygen atmosphere. And the Chemiluminescent image was acquired by a multi-modal in vivo imaging system (Kodak In-Vivo FX Pro, Carestream).

Hydrolysis: 0.1 ml methanol/DMF (8:2) mixture solution of XA-O ( $1.0 \times 10^{-3}$  M) was injected into cell culture plate (96 cell) containing 0.1 ml methanol/water (8:2) mixture solution with sodium methoxide ( $2.0 \times 10^{-2}$  M) under oxygen atmosphere. And the Chemiluminescent image was acquired by a multi-modal in vivo imaging system (Kodak In-Vivo FX Pro, Carestream).

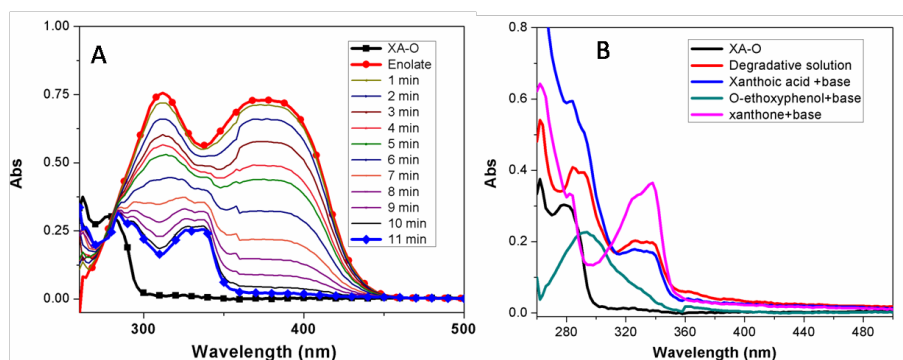
### **The degradation procedure of XA-O or XA-C under $^{18}\text{O}_2$ atmosphere:**

3 ml of DMF (spectrum pure) was added into schlenk flask containing XA-O or XA-C (2 mmol) and base (20 eq) under nitrogen atmosphere, and stirred for 10 minutes. Then  $^{18}\text{O}_2$  gas was injected into reaction flask using a syringe. After stirred at room temperature for 1 h, the obtained mixture was performed in positive (negative) ion mode on a Autoflex speed MAIDI-TOF/TOF mass spectrometer.

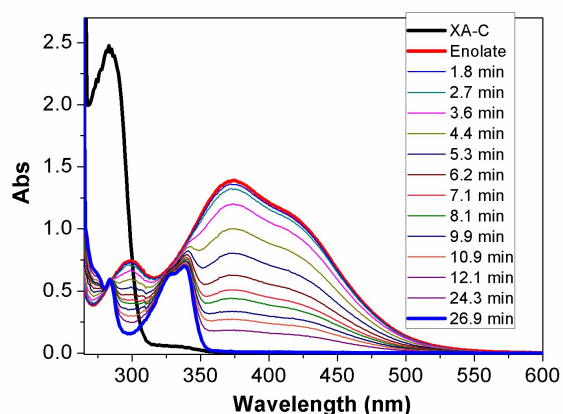
### **Computational details:**

All calculation have been performed by Gaussian09 program. The computation consists of two successive steps: (1) the geometrical parameters are obtained at the UCAM-B3LYP/6-31G(d,p); (2) to check the intrinsic reaction coordinate (IRC), to optimize the stationary points (i.e., minimum (Min), TS, and Int), the vibrational spectrum has been calculated to characterize their nature at the same UCAM-B3LYP/6-31G(d,p) level.

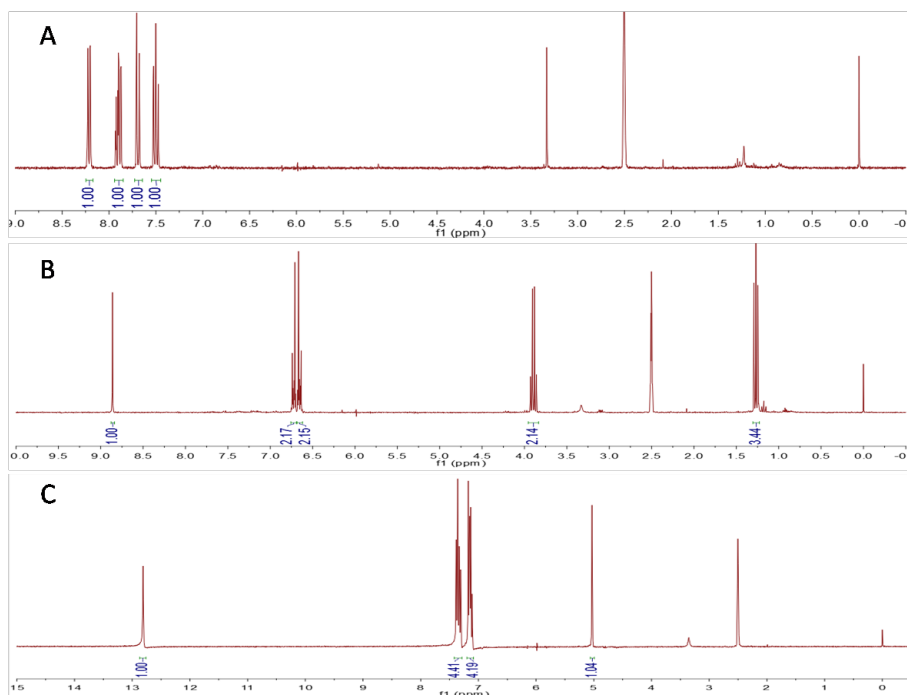
## Supplemental Figures:



**Figure S1 – The time-resolved absorption spectra of XA-O, Related to Figure 1:** (A) Time-resolved absorption spectra of XA-O stimulated by 20 eq potassium tert-butoxide and then exposed to oxygen. Absorption spectra of XA-O (black curve) and enolate form of XA-O (red curve) under a nitrogen atmosphere. (B) The absorption spectra of XA-O (black curve), XA-O after complete degradation (red curve), and xanthoic acid (blue curve), o-ethoxyphenol (green curve) and xanthone (pink curve) in the present of 20 eq Potassium tert-butoxide.

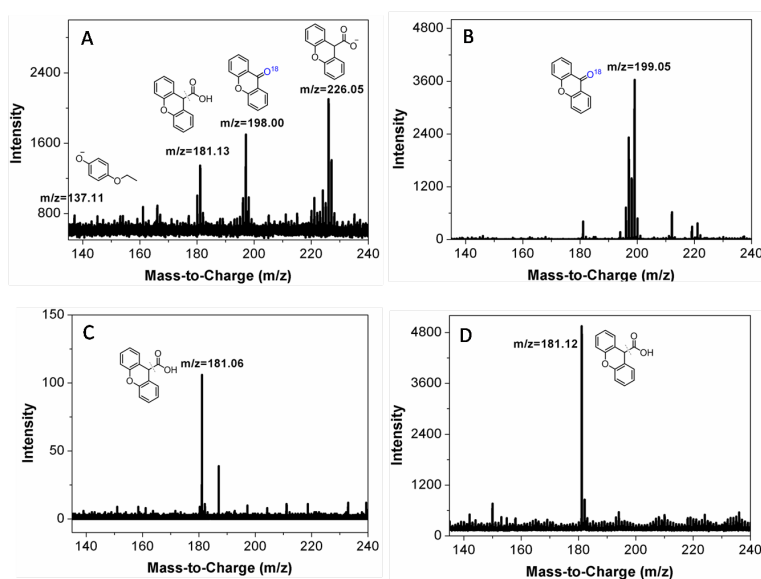


**Figure S2 – The time-resolved absorption spectra of XA-C, Related to Figure 1:** Time-resolved absorption spectra of XA-C stimulated by 20 eq potassium tert-butoxide and then exposed to oxygen. Absorption spectra of XA-C (black curve) and enolate form of XA-C (red curve) under a nitrogen atmosphere.



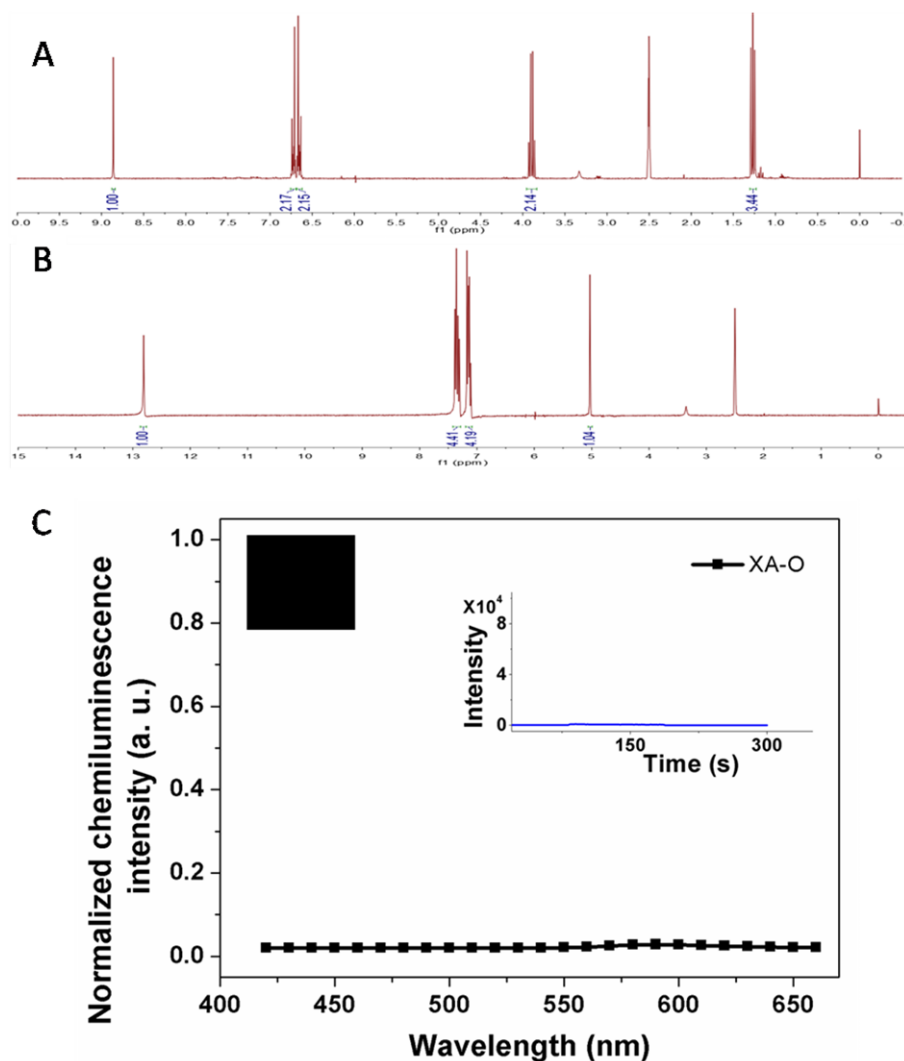
**Figure S3 – The NMR characterization of XA-O's degradation products, Related to Figure 2:**

$^1\text{H}$  NMR spectra of degradation product 1 (A), 2 (B) and 3 (C) which were isolated by column chromatography. Product 1:  $^1\text{H}$  NMR (300 MHz, dmsO)  $\delta$  8.25 – 8.17 (m, 1H), 7.94 – 7.85 (m, 1H), 7.73 – 7.64 (m, 1H), 7.50 (ddd,  $J$  = 8.0, 7.1, 1.1 Hz, 1H). Product 2:  $^1\text{H}$  NMR (300 MHz, dmsO)  $\delta$  8.86 (s, 1H), 6.76 – 6.69 (m, 2H), 6.68 – 6.62 (m, 2H), 3.89 (q,  $J$  = 7.0 Hz, 2H), 1.27 (t,  $J$  = 7.0 Hz, 3H). Product 3:  $^1\text{H}$  NMR (300 MHz, dmsO)  $\delta$  12.81 (s, 1H), 7.35 (dd,  $J$  = 15.3, 7.6 Hz, 4H), 7.20 – 7.09 (m, 4H), 5.03 (s, 1H).



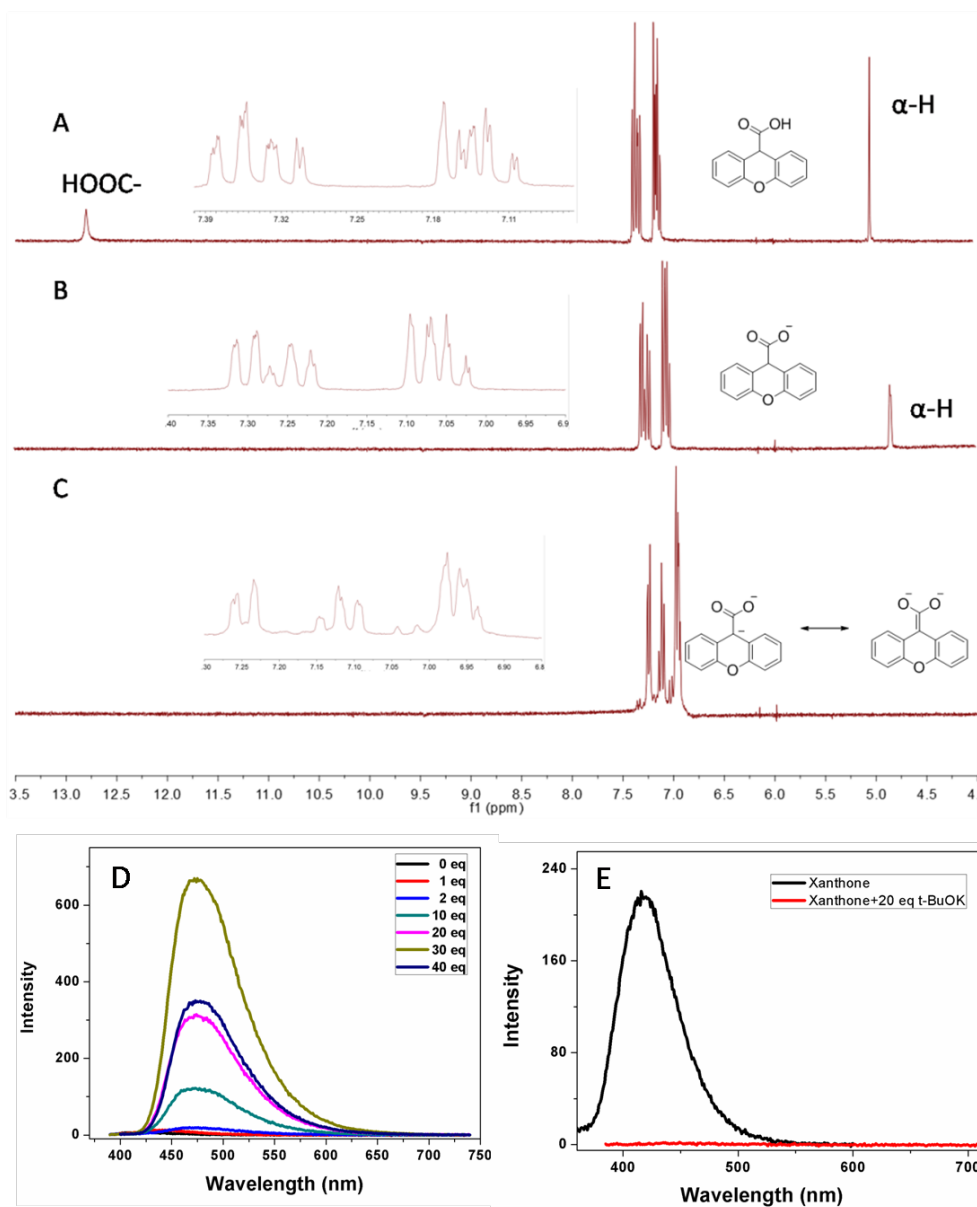
**Figure S4 –The MS characterization of XA-O and XA-C's degradation products, Related to Figure 2: MS of XA-O (negative MS,A), XA-C (positive MS, B) and xanthoic acid (negative MS,**

C; negative MS, D) stimulated by 20 eq potassium tert-butoxide under an  $^{18}\text{O}_2$  atmosphere without further post treatment.

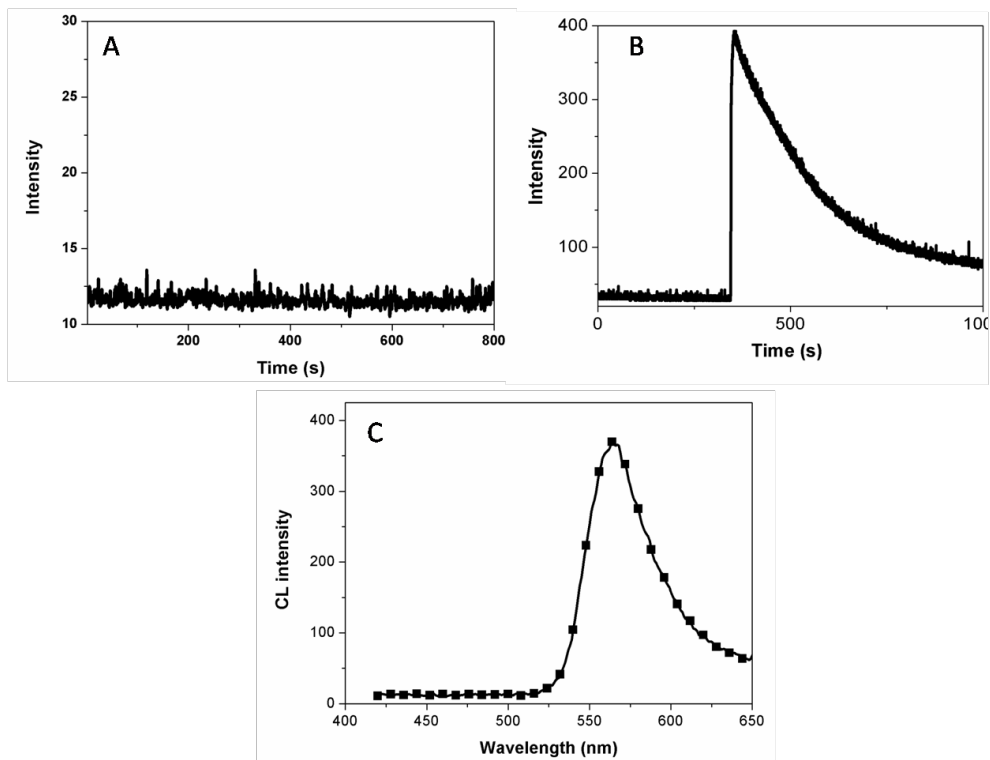


**Figure S5 –The NMR characterization and chemiluminescent property of XA-O's hydrolysis products, Related to Figure 2:**  $^1\text{H}$  NMR spectrum of hydrolysis product 1 (A) and 2 (B) which were isolated by column chromatography. Product 1:  $^1\text{H}$  NMR (300 MHz, dmsO)  $\delta$  8.86 (s, 1H), 6.76 – 6.69 (m, 2H), 6.68 – 6.62 (m, 2H), 3.89 (q,  $J = 7.0$  Hz, 2H), 1.27 (t,  $J = 7.0$  Hz, 3H). Product 2:  $^1\text{H}$  NMR (300 MHz, dmsO)  $\delta$  12.81 (s, 1H), 7.35 (dd,  $J = 15.3, 7.6$  Hz, 4H), 7.20 – 7.09 (m, 4H), 5.03 (s, 1H). (C) The chemiluminescent spectrum of XA-O stimulated by 20 eq potassium tert-butoxide in methanol/water (4:1) mixture solution under oxygen atmosphere.

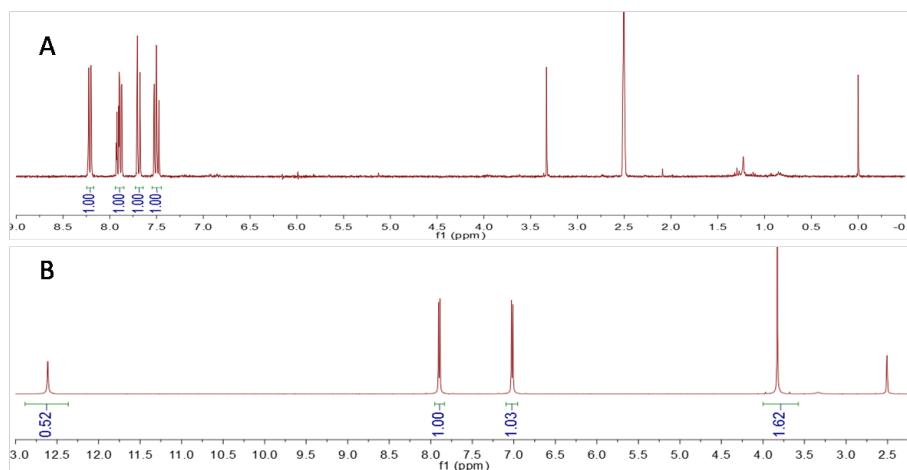




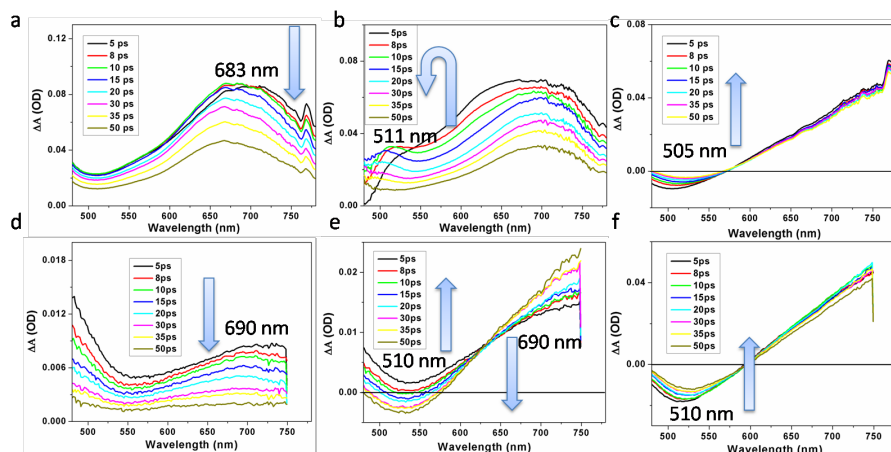
**Figure S6 –The characterization of xanthonic acid, Related to Figure 2:**  $^1\text{H-NMR}$  spectra of xanthonic acid with 0 eq (A), 2 eq (B) and 20 eq (C) potassium tert-butoxide in DMSO- $d_6$ . Fluorescence spectra of xanthonic acid (D) and xanthone (E) with different concentration potassium tert-butoxide in DMF.



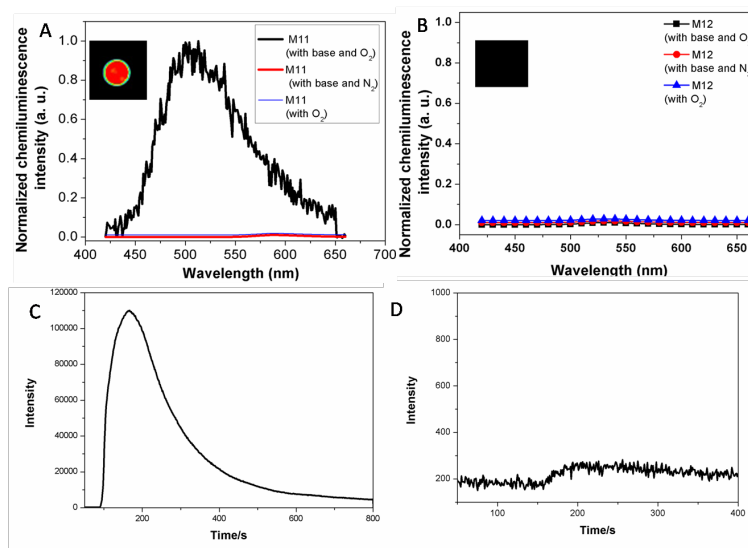
**Figure S7 –The Chemiluminescent property of XA-O under an anhydrous condition, Related to Figure 2:** The chemiluminescent kinetic curves of XA-O (A) mixed fluorescein (B), and the chemiluminescent spectrum of XA-O and fluorescein mixture (C) stimulated by 20 eq Potassium tert-butoxide under oxygen atmosphere in anhydrous DMF solution.



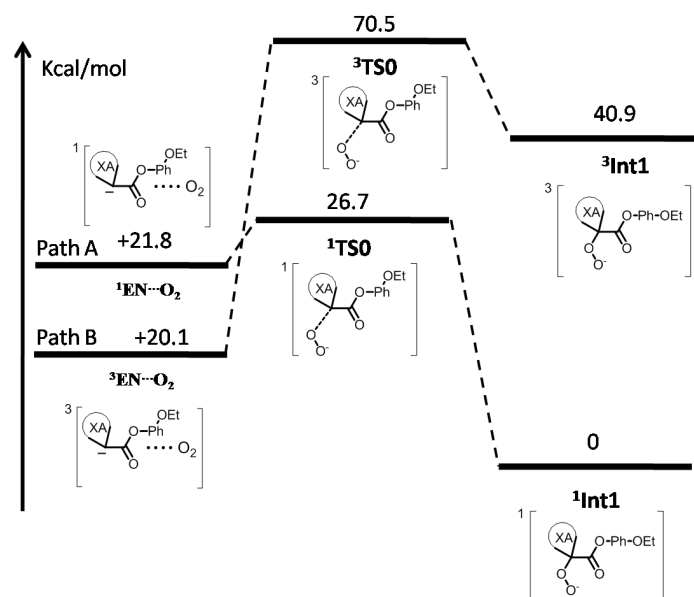
**Figure S8 – The NMR characterization of XA-C's degradation products, Related to Figure 2:** <sup>1</sup>H NMR spectrum of degradation product 1 (A) and 2 (B) which were isolated by column chromatography. Product 1: <sup>1</sup>H NMR (300 MHz, dmsd)  $\delta$  8.25 – 8.17 (m, 1H), 7.94 – 7.85 (m, 1H), 7.73 – 7.64 (m, 1H), 7.50 (ddd,  $J$  = 8.0, 7.1, 1.1 Hz, 1H). Product 2: <sup>1</sup>H NMR (500 MHz, DMSO)  $\delta$  = 12.61 (s, 1H), 7.90 (d,  $J$ =8.8, 2H), 7.02 (d,  $J$ =8.8, 2H), 3.83 (s, 2H).



**Figure S9 –The FTAS characterization of M11 and M12, Related to Figure 2 and Figure 3:** FTAS of M11 (a, b, c) and M12 (d, e, f) before (a, d), after (c, f) and during degradation in the present of 20 eq Potassium tert-butoxide and oxygen. A new peak of FTAS at 511 nm was detected in the ED process of **M11**, compared to the spectra of the enolate form with a peak at 683 nm and the ED product with a peak at 505 nm. In addition, a similar new peak was not found in the ED process of **M12**, compared to the spectra of the enolate form and the ED product. Those indicated that the 511 nm peak of **M11** maybe be assigned to the transient absorption peak of the excited state of the dioxetanone.

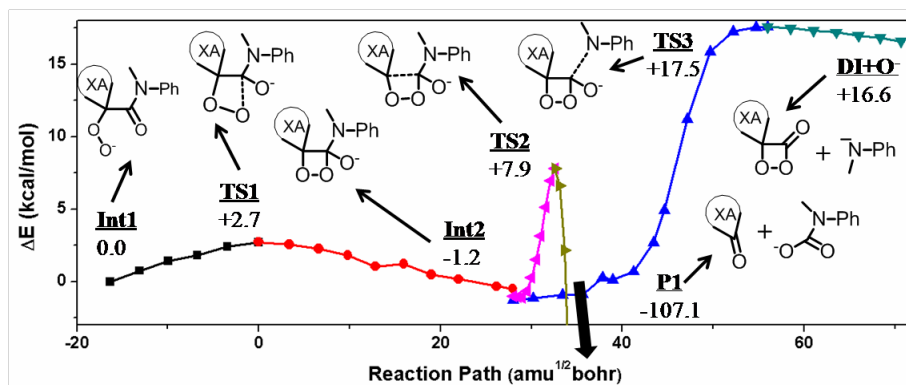


**Figure S10 –The Chemiluminescent properties of M11 and M12, Related to Figure 2 and Figure 3:** The chemiluminescent spectra and kinetic curves of M11 (A, C) and M12 (B, D) stimulated by 20 eq Potassium tert-butoxide under oxygen (black curve), 20 eq Potassium tert-butoxide alone (red curve), and oxygen alone (blue curve).



**Figure S11 –Potential energy surfaces of XA-O's oxygenation reaction, Related to Figure 3:**

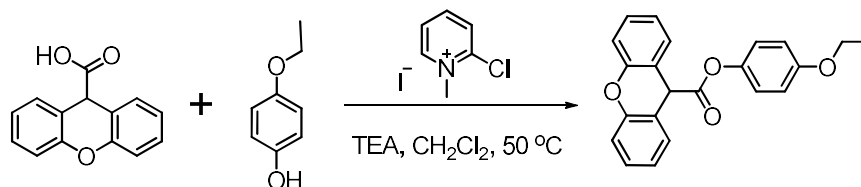
Potential energy surfaces of the reaction of (triplet) oxygen with XA-O. The oxygenation reaction of the XA-O enolate anion (EN) was a spin forbidden process due to that the oxygen was triplet state and enolate/product were single state. Based on many excellent previous works (Liu et al., 2009), two alternative mechanisms were proposed: 1) the singlet state C-O bond was formed via a single electron-transfer mechanism containing a diradical intermediate, denoted as Path A (singlet state) as shown in **Figure S11**; 2) the degradative reaction was triplet state process, denoted as Path B. To further understand of the spin forbidden process of the reaction of (triplet) oxygen with XA-O, DFT method was used to analyze the two paths (A and B) and the structures of intermediates. As shown in Figure S11, XA-O and oxygen complex was firstly formed with weak C-O bond (3.0 Å) in triplet state process. Then, stable C-O bond was formed by crossing over high energy barrier about 50.4 kcal/mol. Simultaneously, O-O bond was increased from 1.2 Å to 2.1 Å, which indicated that O-O bond had become weak and the intermediate was unstable. However, only 4.9 kcal/mol energy barrier should be overcome to gain **Int1** through single electron-transfer mechanism. Compared with the energy barrier and stability of intermediate, we can confirm that the addition reaction of (triplet) oxygen with XA-O was single electron-transfer mechanism, similar to that of luciferin.



**Figure S12 –Potential energy surface of M5, Related to Figure 3:** Potential energy surface of the generation and degradation taking different pathways for M5 computed at the UCAM-B3LYP/6-31G(d,p) level.

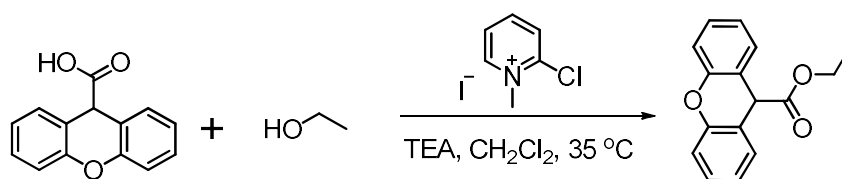


## Synthesis of XA-O, XA-C, and M3-M18.

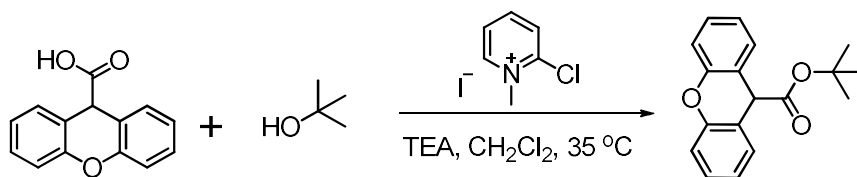


The general synthetic procedure for XA-O, M3, M4, M6, M7, and M13-M18 using XA-O as a template is as follows:

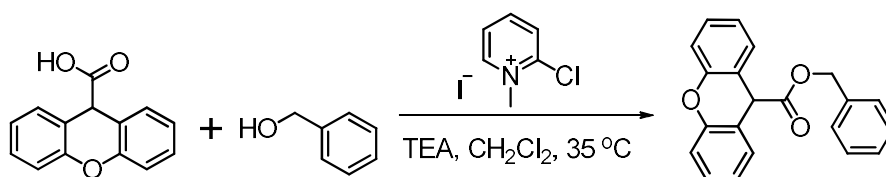
**4-ethoxyphenyl 9H-xanthene-9-carboxylate (XA-O):** Xanthene-9-carboxylic acid (1.13 g, 5 mmol) and 4-ethoxyphenol (0.69 g, 5 mmol) was added to the solution of dry  $\text{CH}_2\text{Cl}_2$  (30 ml) and triethylamine (4 ml) containing 2-chloro-1-methylpyridinium (1.9 g, 7.5 mmol). After stirring for 6 h at 50 °C, the reaction mixture was concentrated under reduced pressure. The crude residue was dissolved to ethyl acetate (35 ml), then filtered. The filter solution was concentrated under reduced pressure, and the white crystal was obtained by a silica-gel column using ethyl acetate/n-hexane mixture (1/100 v/v) as eluent (1.45 g, yield 85%).  $^1\text{H}$  NMR (500 MHz, DMSO)  $\delta$  7.54 (d,  $J = 7.4$  Hz, 2H), 7.40 (t,  $J = 7.5$  Hz, 2H), 7.22 (dd,  $J = 11.7, 7.9$  Hz, 4H), 6.90 (d,  $J = 9.6$  Hz, 4H), 5.48 (s, 1H), 3.97 (q,  $J = 6.9$  Hz, 2H), 1.29 (t,  $J = 6.9$  Hz, 3H).  $^{13}\text{C}$  NMR (125 MHz, DMSO)  $\delta$  170.92, 156.77, 151.29, 144.07, 130.01, 129.93, 124.18, 122.49, 118.57, 117.11, 115.43, 63.83, 44.40, 15.04. LC-HRMS:  $m/z$  calc. for  $\text{C}_{22}\text{H}_{19}\text{O}_4$  347.1283, found 347.1277. m.p.: 143.6-144.5 °C.



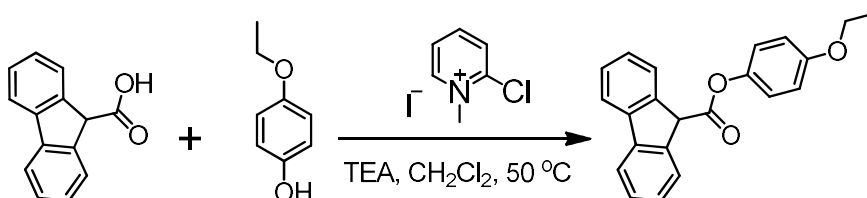
**Ethyl 9H-xanthene-9-carboxylate (M3):** The white powder (85%).  $^1\text{H}$  NMR (500 MHz, DMSO)  $\delta$  7.35 (t,  $J = 7.9$  Hz, 4H), 7.18 (d,  $J = 7.9$  Hz, 2H), 7.14 (t,  $J = 7.4$  Hz, 2H), 5.18 (s, 1H), 4.05 (q,  $J = 7.0$  Hz, 2H), 1.10 (t,  $J = 7.1$  Hz, 3H).  $^{13}\text{C}$  NMR (126 MHz, DMSO)  $\delta$  171.82, 151.25, 129.78, 129.63, 123.98, 119.11, 116.96, 61.57, 44.55, 14.36. LC-HRMS:  $m/z$  calc. for  $\text{C}_{16}\text{H}_{15}\text{O}_3$  255.1021, found 255.1020. m.p.: 64.7- 65.3 °C.



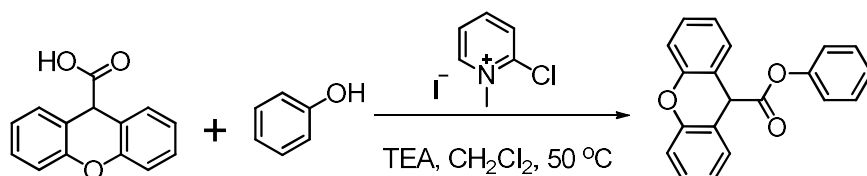
**tert-butyl 9H-xanthene-9-carboxylate (M4):** The white oil (yield 65%).  $^1\text{H}$  NMR (500 MHz, DMSO)  $\delta$  7.33 (t,  $J = 7.2$  Hz, 4H), 7.19 – 7.10 (m, 4H), 5.02 (s, 1H), 1.31 (s, 9H).  $^{13}\text{C}$  NMR (126 MHz, DMSO)  $\delta$  171.12, 151.18, 129.64, 129.47, 123.86, 119.36, 116.87, 81.63, 45.60, 27.90. LC-HRMS:  $m/z$  calc. for  $\text{C}_{18}\text{H}_{19}\text{O}_3$  283.1334, found 283.1340.



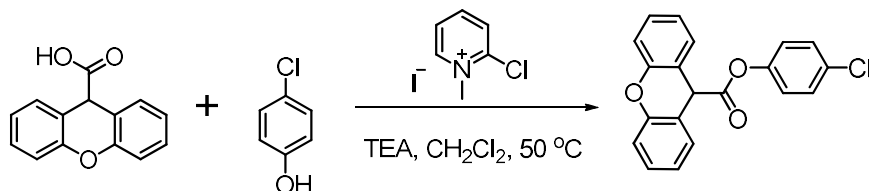
**Benzyl 9H-xanthene-9-carboxylate (M6):** The white powder (55%).  $^1\text{H}$  NMR (500 MHz, DMSO)  $\delta$  7.36 (t,  $J = 9.6$  Hz, 4H), 7.29 (s, 3H), 7.22 – 7.09 (m, 6H), 5.28 (s, 1H), 5.08 (s, 2H).  $^{13}\text{C}$  NMR (126 MHz, DMSO)  $\delta$  171.53, 151.35, 136.30, 129.88, 129.71, 128.81, 128.40, 127.68, 124.00, 119.06, 116.99, 66.75, 44.63. LC-HRMS:  $m/z$  calc. for  $\text{C}_{21}\text{H}_{17}\text{O}_3$  317.1178, found 317.1180. m.p.: 66.7 - 67.4 °C.



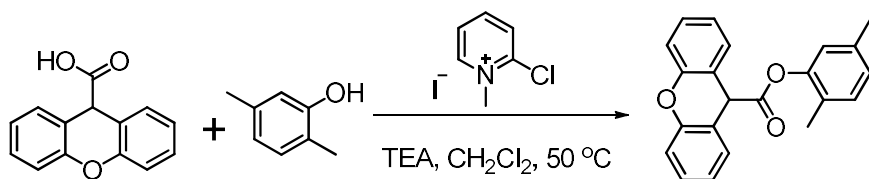
**4-Ethoxyphenyl 9H-fluorene-9-carboxylate (M7):** The white powder (1.23 g, yield 75%).  $^1\text{H}$  NMR (500 MHz, DMSO)  $\delta$  7.95 (d,  $J = 7.4$  Hz, 2H), 7.80 (d,  $J = 7.3$  Hz, 2H), 7.49 (t,  $J = 7.2$  Hz, 2H), 7.42 (t,  $J = 7.3$  Hz, 2H), 7.06 (d,  $J = 8.5$  Hz, 2H), 6.93 (d,  $J = 8.5$  Hz, 2H), 5.35 (s, 1H), 3.99 (dd,  $J = 13.4, 6.6$  Hz, 2H), 1.31 (t,  $J = 6.7$  Hz, 3H).  $^{13}\text{C}$  NMR (125 MHz, DMSO)  $\delta$  170.06, 156.78, 144.20, 141.43, 140.90, 128.78, 128.09, 126.14, 122.84, 120.84, 115.45, 63.85, 53.17, 15.08. LC-HRMS:  $m/z$  calc. for  $\text{C}_{22}\text{H}_{19}\text{O}_3$  331.1334, found 331.1335. m.p.: 123.4 - 124.3 °C.



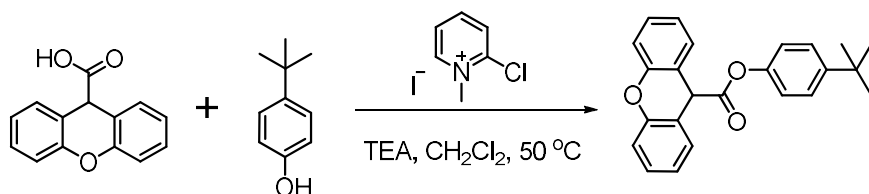
**Phenyl 9H-xanthene-9-carboxylate (M13):** The white powder (2.7 g, yield 90%).  $^1\text{H}$  NMR (500 MHz, DMSO)  $\delta$  7.56 (d,  $J = 7.4$  Hz, 2H), 7.45 – 7.34 (m, 4H), 7.29 – 7.18 (m, 5H), 6.98 (d,  $J = 7.9$  Hz, 2H), 5.52 (s, 1H).  $^{13}\text{C}$  NMR (125 MHz, DMSO)  $\delta$  170.60, 151.41, 150.81, 130.10, 130.03, 129.97, 126.62, 124.20, 121.68, 118.50, 117.13, 44.46. LC-HRMS:  $m/z$  calc. for  $\text{C}_{20}\text{H}_{15}\text{O}_3$  303.1021, found 303.1020. m.p.: 112.5 - 113.3°C.



**4-chlorophenyl 9H-xanthene-9-carboxylate (M14):** ethyl acetate/n-hexane (1/50 v/v) as eluent to obtain the white powder (2.18 g, yield 60%).  $^1\text{H}$  NMR (500 MHz, DMSO)  $\delta$  7.47 – 7.37 (m, 4H), 7.22 (dd,  $J = 12.3, 7.7$  Hz, 4H), 7.04 (d,  $J = 8.8$  Hz, 2H), 5.53 (s, 1H).  $^{13}\text{C}$  NMR (125 MHz, DMSO)  $\delta$  170.44, 151.32, 149.52, 130.77, 130.09, 130.04, 130.02, 124.22, 123.68, 118.32, 117.14, 44.35. LC-HRMS:  $m/z$  calc. for  $\text{C}_{20}\text{H}_{14}\text{ClO}_3$  337.0631, found 337.0639. m.p.: 93.5 - 94.4°C.

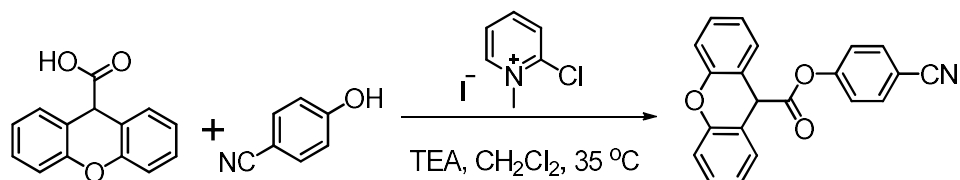


**2,5-dimethylphenyl 9H-xanthene-9-carboxylate (M15):** ethyl acetate/n-hexane (1/100 v/v) as eluent to obtain the white powder (3.0 g, yield 91%).  $^1\text{H}$  NMR (500 MHz, DMSO)  $\delta$  7.54 (d,  $J = 7.4$  Hz, 2H), 7.40 (t,  $J = 7.3$  Hz, 2H), 7.22 (dd,  $J = 14.5, 7.6$  Hz, 4H), 7.07 (d,  $J = 7.7$  Hz, 1H), 6.93 (d,  $J = 7.6$  Hz, 1H), 6.68 (s, 1H), 5.50 (s, 1H), 2.21 (s, 3H), 1.71 (s, 3H).  $^{13}\text{C}$  NMR (126 MHz, DMSO)  $\delta$  170.09, 151.41, 149.06, 137.05, 131.24, 129.98, 127.31, 126.68, 124.16, 122.30, 118.75, 117.11, 44.66, 20.71, 15.09. LC-HRMS:  $m/z$  calc. for  $\text{C}_{22}\text{H}_{19}\text{O}_3$  331.1334, found 331.1330. m.p.: 111.1-111.6°C.

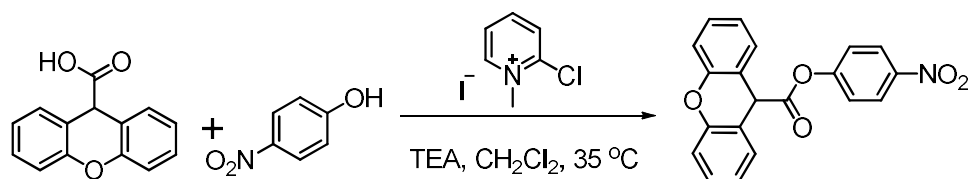


**4-(tert-butyl)phenyl 9H-xanthene-9-carboxylate (M16):** ethyl acetate/n-hexane (1/100 v/v) as eluent to obtain the white powder (3.0 g, yield 85%).  $^1\text{H}$  NMR (500 MHz, DMSO)  $\delta$  7.54 (d,  $J = 7.4$  Hz, 2H), 7.39 (dd,  $J = 16.2, 8.5$  Hz, 4H), 7.21 (dd,  $J = 12.2, 7.7$  Hz, 4H), 6.88 (d,  $J = 8.7$  Hz,

2H), 5.50 (s, 1H), 1.24 (s, 9H).  $^{13}\text{C}$  NMR (125 MHz, DMSO)  $\delta$  170.69, 151.31, 148.97, 148.56, 130.00, 129.94, 126.76, 124.18, 121.03, 118.54, 117.12, 44.47, 34.66, 31.57. LC-HRMS:  $m/z$  calc. for  $\text{C}_{24}\text{H}_{23}\text{O}_3$  359.1647, found 359.1640. m.p.: 96.6 - 97.5°C.

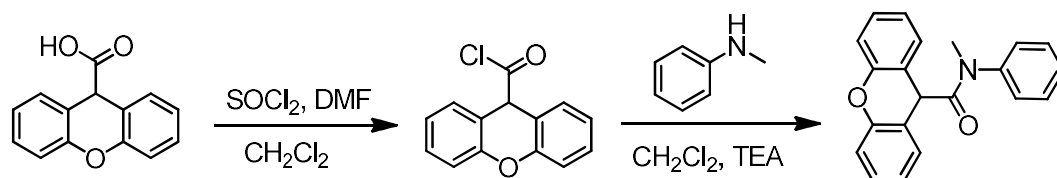


**4-cyanophenyl 9H-xanthene-9-carboxylate (M17):** Ethyl acetate/n-hexane (1/50 v/v) as eluent to obtain the white powder (0.8 g, yield 50%).  $^1\text{H}$  NMR (500 MHz, DMSO)  $\delta$  7.89 (d,  $J = 8.7$  Hz, 2H), 7.58 (d,  $J = 7.3$  Hz, 2H), 7.45 – 7.38 (m, 2H), 7.27 – 7.19 (m, 6H), 5.58 (s, 1H).  $^{13}\text{C}$  NMR (126 MHz, DMSO)  $\delta$  170.01, 154.11, 151.34, 134.68, 130.18, 130.10, 124.25, 123.23, 118.62, 118.12, 117.16, 109.62, 44.36. LC-HRMS:  $m/z$  calc. for  $\text{C}_{21}\text{H}_{14}\text{NO}_3$  328.0974, found 328.0974. m.p.: 93.6 - 94.2 °C.



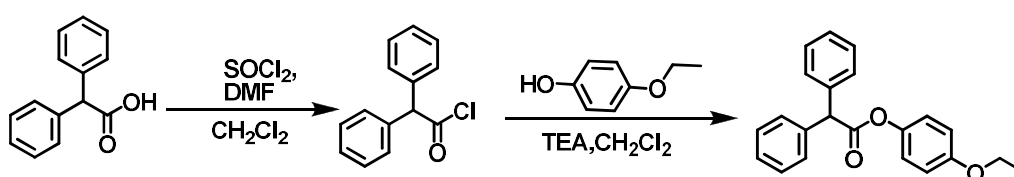
**4-nitrophenyl 9H-xanthene-9-carboxylate (M18):** Ethyl acetate/n-hexane (1/100 v/v) as eluent to obtain the white powder (0.76 g, yield 45%).  $^1\text{H}$  NMR (500 MHz, DMSO)  $\delta$  8.27 (d,  $J = 9.1$  Hz, 2H), 7.60 (d,  $J = 7.0$  Hz, 2H), 7.46 – 7.38 (m, 2H), 7.33 – 7.29 (m, 2H), 7.26 – 7.21 (m, 4H), 5.61 (s, 1H).  $^{13}\text{C}$  NMR (126 MHz, DMSO)  $\delta$  169.92, 155.46, 151.37, 145.71, 130.20, 130.13, 125.92, 124.27, 123.19, 118.09, 117.18, 44.38. LC-HRMS:  $m/z$  calc. for  $\text{C}_{20}\text{H}_{14}\text{NO}_5$  348.0872, found 348.0870. m.p.: 116.4 - 117.3 °C.

**The general synthetic procedure for M5 and M8 using M5 as a template is as follows:**



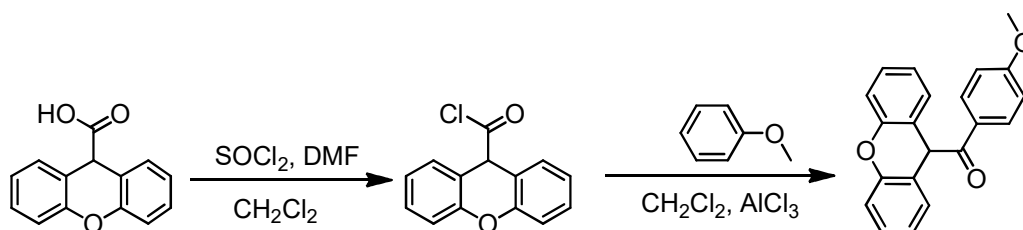
**N-methyl-N-phenyl-9H-xanthene-9-carboxamide (M5):** The mixture solution of 40 ml  $\text{CH}_2\text{Cl}_2$ , 0.2 ml DMF and 1.5 ml  $\text{SOCl}_2$  containing 9H-xanthene-9-carboxylic acid (2.26 g, 10 mmol) was stirred at room temperature for 2 h. Then, the reaction mixture was concentrated under reduced pressure. The crude residue was dissolved to the mixture solution of  $\text{CH}_2\text{Cl}_2$  (35 ml) and

triethylamine (4 ml) containing N-methylaniline (1.1 g, 10 mmol), then stirred at room temperature for 6 h. The reaction mixture was concentrated under reduced pressure, and the crude residue was dissolved subsequently to the ethyl acetate (50 ml), then filtered. After concentrated under reduced pressure, the purified crystal was obtained (2.82 g, yield 85%). <sup>1</sup>H NMR (500 MHz, DMSO) δ 7.54 (d, *J* = 7.4 Hz, 2H), 7.39 (dd, *J* = 16.2, 8.5 Hz, 4H), 7.21 (dd, *J* = 12.2, 7.7 Hz, 4H), 6.88 (d, *J* = 8.7 Hz, 2H), 5.50 (s, 1H), 1.24 (s, 9H). <sup>13</sup>C NMR (125 MHz, DMSO) δ 171.43, 151.55, 142.91, 130.71, 129.11, 128.82, 128.75, 128.52, 123.81, 120.76, 116.95, 41.39, 38.19. LC-HRMS: *m/z* calc. for C<sub>21</sub>H<sub>18</sub>NO<sub>2</sub> 316.1338, found 316.1338. m.p.: 155.0 - 155.8°C.



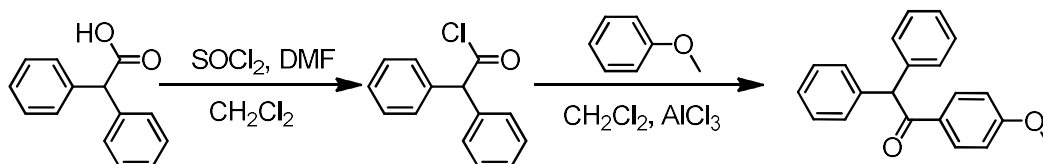
**4-ethoxyphenyl 2,2-diphenylacetate (M8):** the white powder (2.82 g, yield 85%) <sup>1</sup>H NMR (500 MHz, DMSO) δ 7.46 – 7.33 (m, 8H), 7.29 (t, *J* = 7.1 Hz, 2H), 6.99 (d, *J* = 8.9 Hz, 2H), 6.93 (d, *J* = 8.9 Hz, 2H), 5.49 (s, 1H), 3.99 (q, *J* = 6.9 Hz, 2H), 1.30 (t, *J* = 6.9 Hz, 3H). <sup>13</sup>C NMR (125 MHz, DMSO) δ 171.68, 156.75, 144.13, 139.16, 129.14, 129.00, 127.71, 122.74, 115.46, 63.84, 56.05, 15.07. LC-HRMS: *m/z* calc. for C<sub>22</sub>H<sub>20</sub>O<sub>3</sub>333.1491, found 333.1497. m.p.: 76.4-77.3°C.

**The general synthetic procedure for XA-C and M9 using XA-C as a template is as follows:**



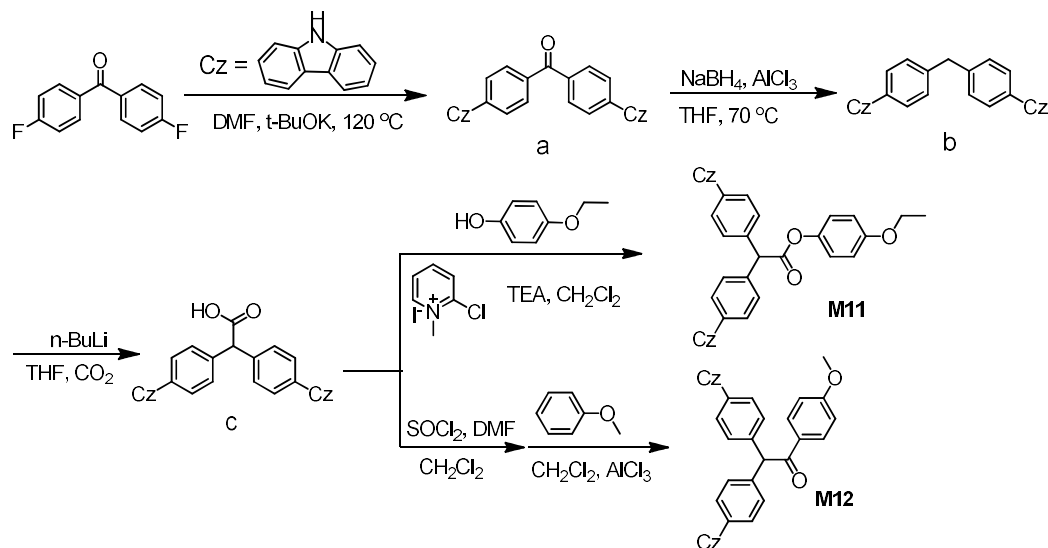
**(4-Methoxyphenyl)(9H-xanthen-9-yl)methanone (XA-C):** The mixture solution of CH<sub>2</sub>Cl<sub>2</sub> (40 ml), DMF (0.2 ml), SOCl<sub>2</sub> (1.5 ml) and xanthene-9-carboxylic acid (2.12 g, 10 mmol) was stirred for 2 h at room temperature. The reaction mixture was concentrated under reduced pressure. Then, the crude residue was dissolved to the solution of CH<sub>2</sub>Cl<sub>2</sub> (35 ml) containing anisole (10 ml) and AlCl<sub>3</sub> (3.2 g) in the ice-water, following stirred at room temperature for additional 6 h. Subsequently, reaction mixture was poured into water (20 ml), then washed with EtOAc (3 times). The combined organic layers were washed with brine and dried over MgSO<sub>4</sub>. After being filtered and concentrated in vacuum, the crude product was purified by a silica-gel column using ethyl

acetate/n-hexane mixture (1/200 v/v) as eluent (1.9 g, yield 60%).  $^1\text{H}$  NMR (500 MHz,  $\text{CDCl}_3$ )  $\delta$  7.94 (d,  $J = 8.9$  Hz, 2H), 7.23 (d,  $J = 7.2$  Hz, 2H), 7.16 (d,  $J = 8.1$  Hz, 2H), 7.11 (d,  $J = 7.5$  Hz, 2H), 6.96 (t,  $J = 7.4$  Hz, 2H), 6.86 (d,  $J = 8.9$  Hz, 2H), 5.75 (s, 1H), 3.81 (s, 3H).  $^{13}\text{C}$  NMR (125 MHz,  $\text{CDCl}_3$ )  $\delta$  196.32, 163.44, 150.81, 131.94, 128.90, 128.63, 128.10, 123.32, 119.55, 117.22, 113.90, 55.44, 48.42. LC-HRMS:  $m/z$  calc. for  $\text{C}_{21}\text{H}_{17}\text{O}_3$  317.1178, found 317.1173. m.p.: 113.8 - 114.6°C.



**1-(4-methoxyphenyl)-2,2-diphenylethanone (M9):** yield 90%.  $^1\text{H}$  NMR (500 MHz, DMSO)  $\delta$  8.04 (d,  $J = 8.8$  Hz, 2H), 7.31 (m, 8H), 7.26 – 7.17 (m, 2H), 7.00 (d,  $J = 8.8$  Hz, 2H), 6.35 (s, 1H), 3.81 (s, 1H).  $^{13}\text{C}$  NMR (126 MHz, DMSO)  $\delta$  196.83, 163.63, 140.22, 131.66, 129.55, 129.47, 128.94, 127.19, 114.45, 57.73, 56.01. LC-HRMS:  $m/z$  calc. for  $\text{C}_{21}\text{H}_{19}\text{O}_2$  303.1385, found 303.1388. m.p.: 121.2 - 122.3°C.

#### Synthetic route of M11 and M12



#### Synthesis of bis(4-(9H-carbazol-9-yl)phenyl)methanone (a)

The carbazole (1.67 g, 10 mmol) and t-BuOK (1.68 g, 15 mmol) was added to the anhydrous DMF (40 mL), and heated to 60 °C for 30 minutes followed by the addition of bis(4-fluorophenyl)methanone (1.09 g, 5 mmol). The reaction mixture was then heated to 120 °C for 12 h. The reaction mixture was poured into water (50 mL). After filtration and washing with

water (100 mL\*3), the solid was dissolved in CH<sub>2</sub>Cl<sub>2</sub>, and then dried over Na<sub>2</sub>SO<sub>4</sub>. The crude product was recrystallized with acetone to obtain a (2.32 g, 91% yield).

#### **Synthesis of bis(4-(9H-carbazol-9-yl)phenyl)methane (b)**

To a stirred solution of NaBH<sub>4</sub> (0.8 g, 20 mmol) in anhydrous THF (40 mL), AlCl<sub>3</sub> (1.6 g, 12 mmol) was added in batches under N<sub>2</sub>. Then, a (1.03 g, 2 mmol) was added to the reaction mixture, and stirred at 70 °C for 20 h. The reaction mixture was poured into ice water (100 mL). After filtration and washing with water (100 mL\*3), the solid was dissolved in CH<sub>2</sub>Cl<sub>2</sub>, then dried over Na<sub>2</sub>SO<sub>4</sub>. The crude product was recrystallized with methanol to obtain b (0.85 g, 85% yield).

#### **Synthesis of 2,2-bis(4-(9H-carbazol-9-yl)phenyl)acetic acid (c)**

To a solution of b (1.0 g, 2 mmol) in 30 mL dry THF, n-butyllithium (2 mL, 5mmol, 2.5 M in n-hexane) was added dropwise at -78 °C under stirring. Dark brown solution was obtained for 2 h under nitrogen. Then, carbon dioxide was injected to the obtained solution. The solution was allowed to warm to room temperature, and stirred for additional 12 h. The solvent was evaporated under reduced pressure. Purify the crude product by a silica-gel column using dichloromethane/methanol mixture (90/10 v/v) as eluent. Yield 50%.

#### **Synthesis of 4-ethoxyphenyl 2,2-bis(4-(9H-carbazol-9-yl)phenyl)acetate (M11)**

C (1.1 g, 2 mmol) and 4-ethoxyphenol (0.28 g, 2 mmol) were added to the mixture solution of dry CH<sub>2</sub>Cl<sub>2</sub> (25 ml) and triethylamine (1ml) containing 4-Ethoxyphenol (0.9 g, 3.5 mmol) under stirring at 50 °C. After 6 h, the reaction mixture was concentrated under reduced pressure, and the crude residue was dissolved to the ethyl acetate (25 ml). After filtered, the filter solution was concentrated under reduced pressure, and the white power was obtained by a silica-gel column (1.0 g, yield 75%). <sup>1</sup>H NMR (500 MHz, DMSO) δ 8.25 (d, *J* = 7.7 Hz, 4H), 7.86 (d, *J* = 8.2 Hz, 4H), 7.71 (d, *J* = 8.2 Hz, 4H), 7.46 – 7.37 (m, 8H), 7.29 (dd, *J* = 9.5, 3.9 Hz, 4H), 7.14 (d, *J* = 8.9 Hz, 2H), 6.98 (d, *J* = 8.9 Hz, 2H), 5.89 (s, 1H), 4.02 (q, *J* = 6.9 Hz, 2H), 1.32 (t, *J* = 6.9 Hz, 3H). <sup>13</sup>CNMR (500 MHz, DMSO) δ 171.56, 156.88, 130.89, 127.35, 126.74, 123.27, 122.90, 120.99, 120.61, 115.52, 110.20, 63.88, 55.26, 15.09. LC-HRMS: *m/z* calc. for C<sub>46</sub>H<sub>35</sub>N<sub>2</sub>O<sub>3</sub> 663.2648, found 663.2643. m.p.: 109.7 - 110.6 °C.

#### **Synthesis of 2,2-bis(4-(9H-carbazol-9-yl)phenyl)-1-(4-methoxyphenyl)ethanone (M12)**

The mixture solution of CH<sub>2</sub>Cl<sub>2</sub> (20 ml), DMF (0.1 ml), SOCl<sub>2</sub> (0.15 ml) and xanthene-9-carboxylic acid (0.162 g, 0.3 mmol) was stirred at room temperature. After 2h, the

reaction mixture was concentrated under reduced pressure. Then, the crude residue was dissolved to the solution of  $\text{CH}_2\text{Cl}_2$  (20 ml) containing anisole (1 ml) and  $\text{AlCl}_3$  (0.3 g) in the ice-water under stirring. After stirred for 6 h at room temperature, the reaction mixture was poured into water (20 ml), then washed with EtOAc (3 times). Then, the combined organic layers were washed with brine and dried over  $\text{MgSO}_4$ . After being filtered and concentrated in vacuum, the crude product was purified by a silica-gel column using ethyl acetate/n-hexane mixture (1/40 v/v) as eluent (65 mg, yield 35%).  $^1\text{H}$  NMR (500 MHz,  $\text{CDCl}_3$ )  $\delta$  8.17 (d,  $J = 7.1$  Hz, 6H), 7.64 (q,  $J = 8.4$  Hz, 8H), 7.49 (d,  $J = 8.1$  Hz, 4H), 7.43 (t,  $J = 7.5$  Hz, 4H), 7.31 (dd,  $J = 15.0, 7.7$  Hz, 4H), 7.04 (d,  $J = 8.7$  Hz, 2H), 6.29 (s, 1H), 3.93 (s, 3H).  $^{13}\text{C}$  NMR (126 MHz,  $\text{CDCl}_3$ )  $\delta$  181.64, 163.89, 140.74, 138.25, 136.87, 131.48, 130.61, 127.28, 125.94, 123.43, 120.31, 120.02, 120.00, 114.12, 109.87, 58.06, 55.59. LC-HRMS:  $m/z$  calc. for  $\text{C}_{46}\text{H}_{35}\text{N}_2\text{O}_2$  647.2699, found 647.2693.



# $^1\text{H}$ NMR and $^{13}\text{C}$ NMR of XA-O, XA-C, and M3-M18

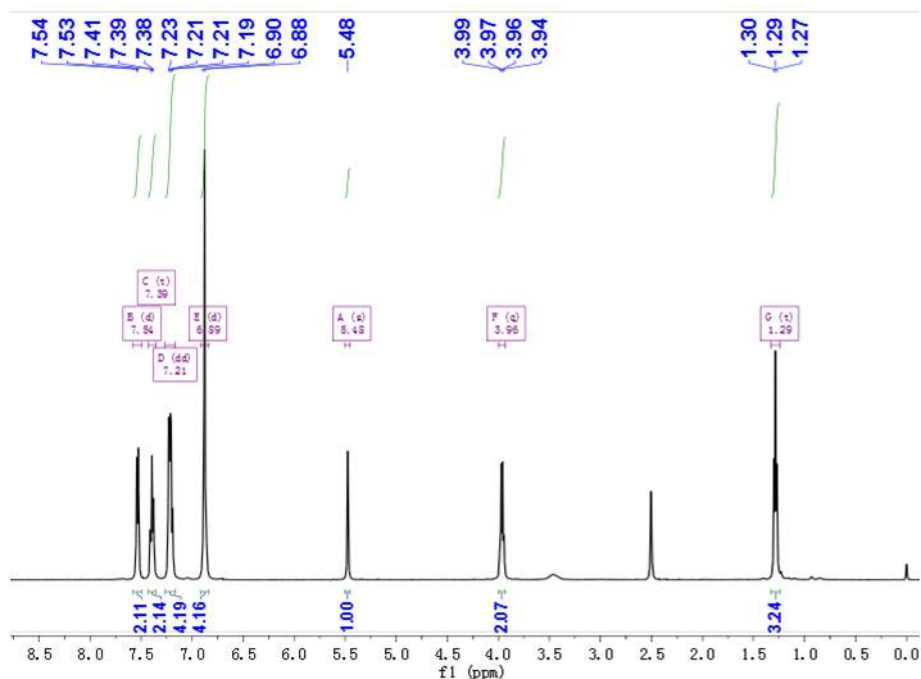


Figure S13 – The  $^1\text{H}$  NMR (500 MHz, DMSO) spectrum of XA-O, Related to Figure 1.



Figure S14 – The  $^{13}\text{C}$  NMR (500 MHz, DMSO) spectrum of XA-O, Related to Figure 1.

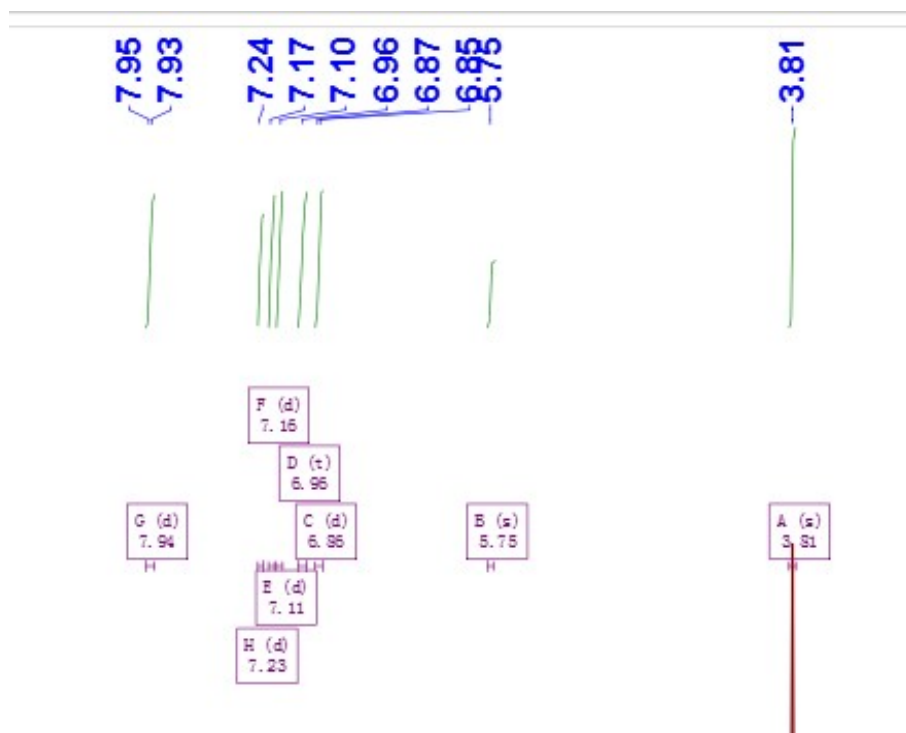


Figure S15 – The  $^1\text{H}$  NMR (500 MHz, DMSO) spectrum of XA-C, Related to Figure 1.

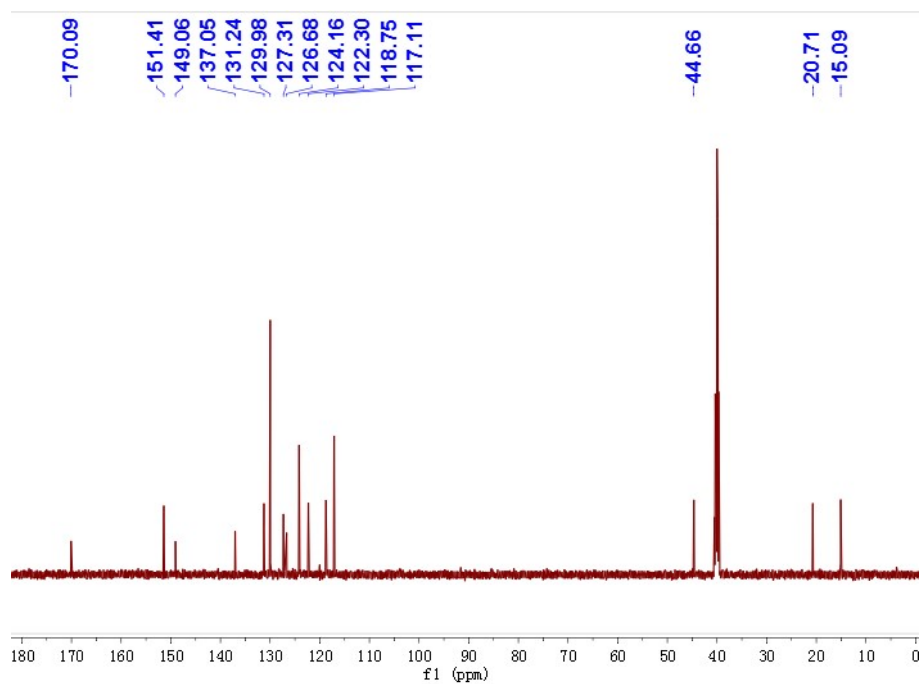


Figure S16 – The  $^{13}\text{C}$  NMR(500 MHz, DMSO) spectrum of XA-C, Related to Figure 1.

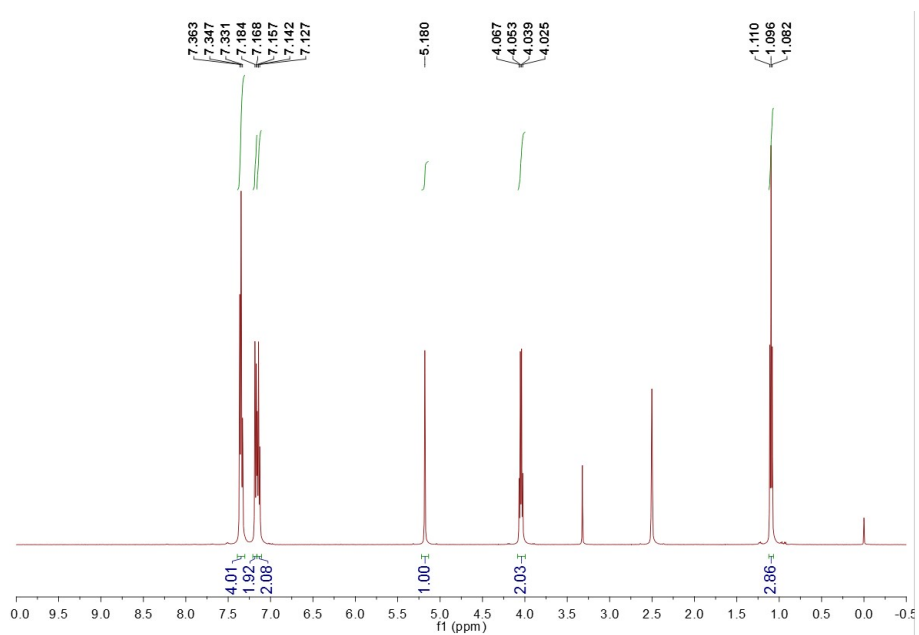


Figure S17 – The  $^1\text{H}$  NMR (500 MHz, DMSO) spectrum of M3, Related to Table 1.

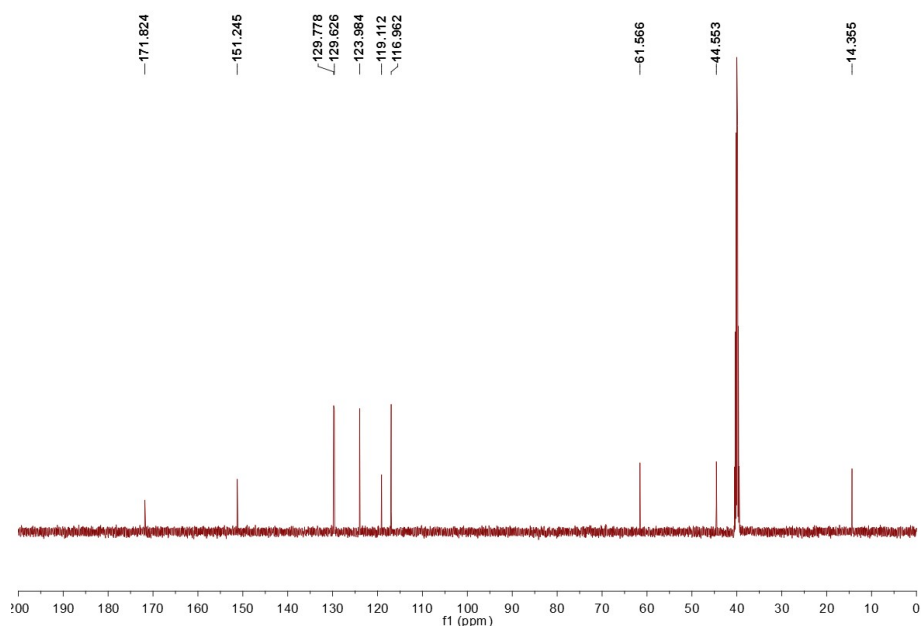


Figure S18 – The  $^{13}\text{C}$  NMR(500 MHz, DMSO) spectrum of M3, Related to Table 1.

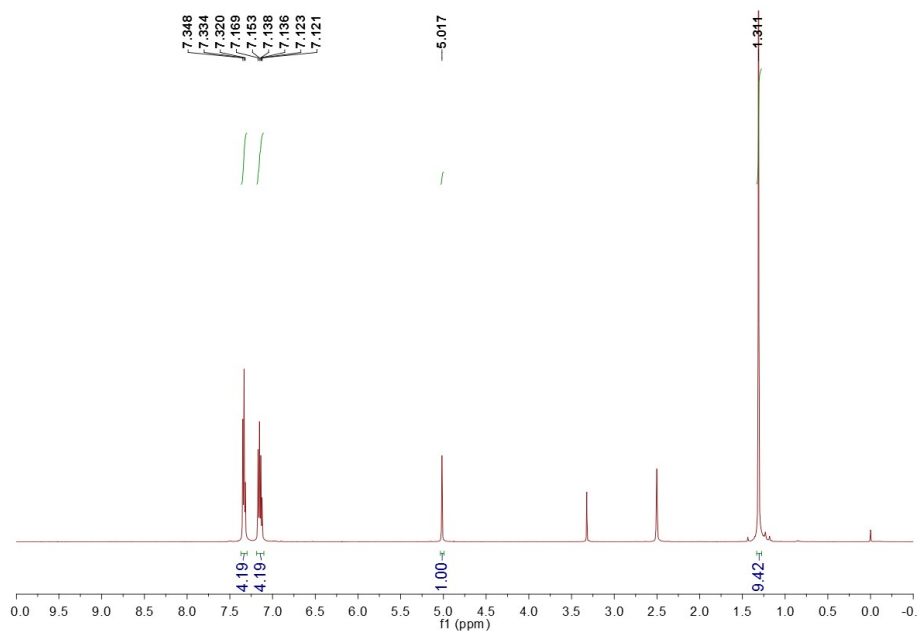


Figure S19 – The  $^1\text{H}$  NMR (500 MHz, DMSO) spectrum of M4, Related to Table 1.

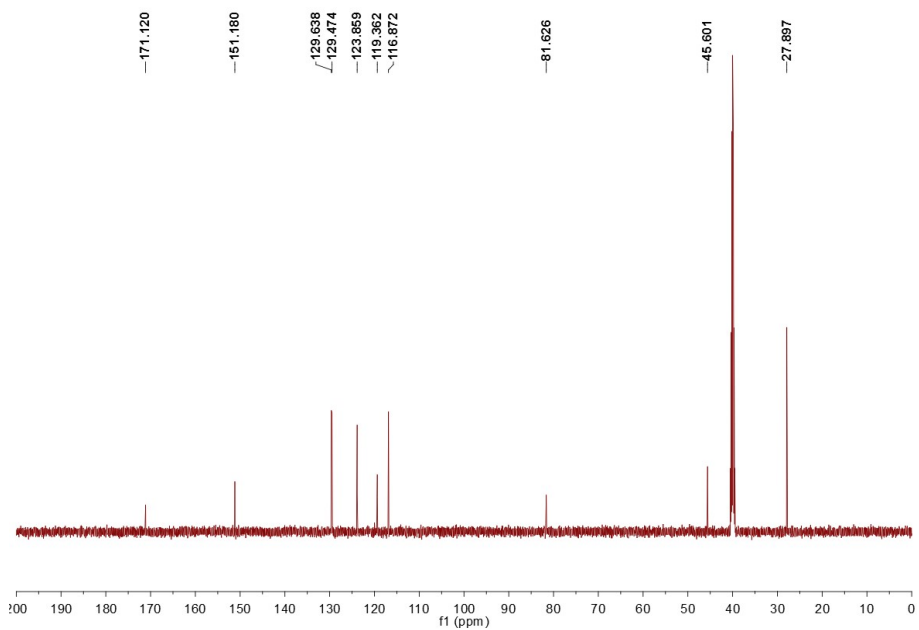


Figure S20 – The  $^{13}\text{C}$  NMR(500 MHz, DMSO) spectrum of M4, Related to Table 1.

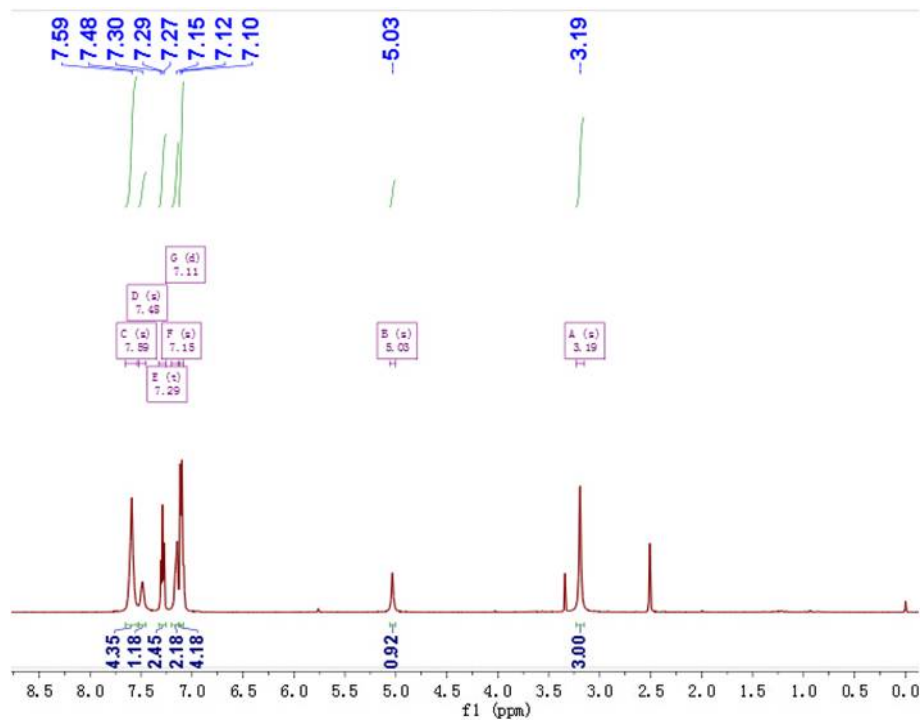


Figure S21 – The  $^1\text{H}$  NMR (500 MHz, DMSO) spectrum of M5, Related to Table 1.

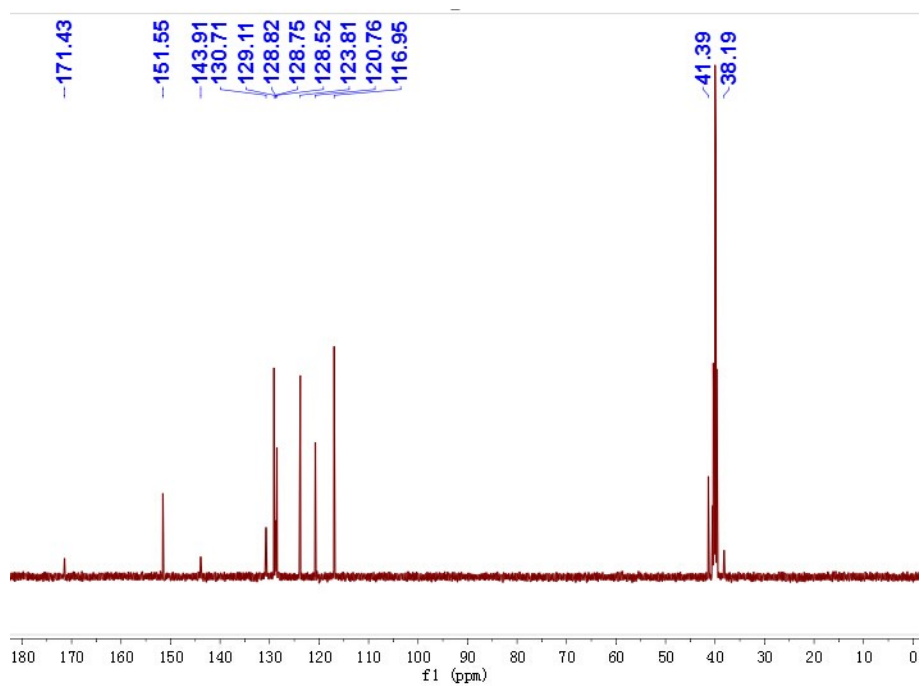
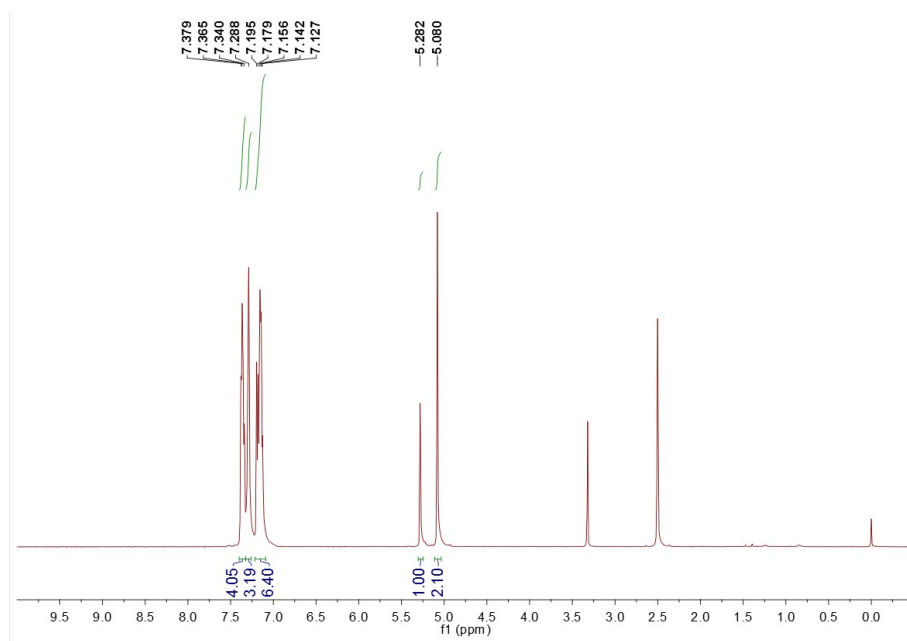
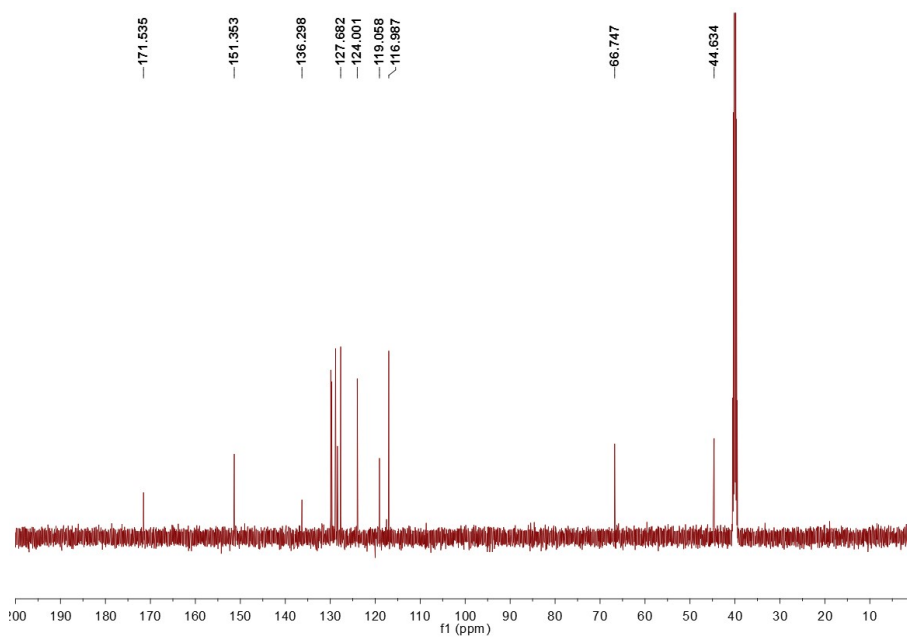


Figure S22 – The  $^{13}\text{C}$  NMR(500 MHz, DMSO) spectrum of M5, Related to Table 1.



**Figure S23 – The  $^1\text{H}$  NMR (500 MHz, DMSO) spectrum of M6, Related to Table 1.**



**Figure S24 – The  $^{13}\text{C}$  NMR (500 MHz, DMSO) spectrum of M6, Related to Table 1.**

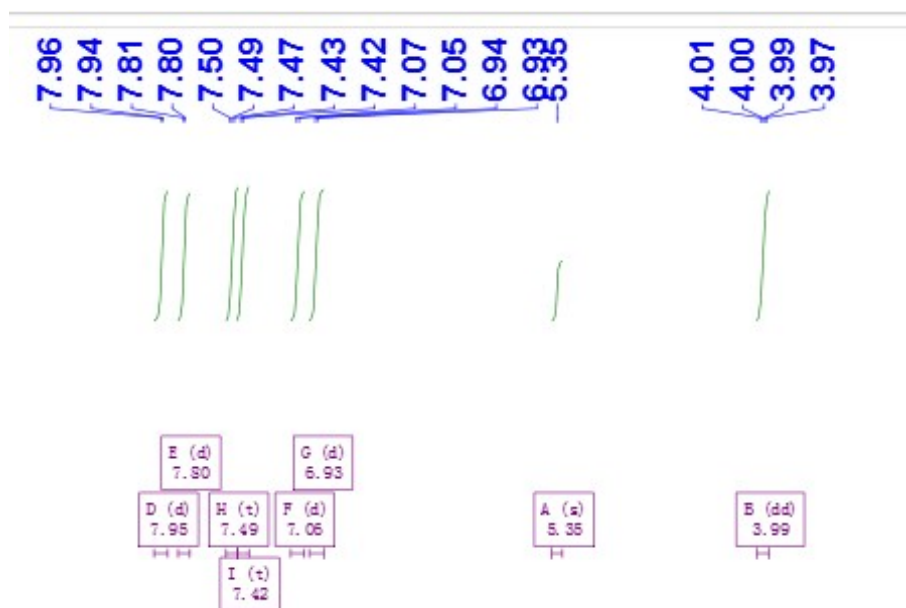


Figure S25 – The  $^1\text{H}$  NMR (500 MHz, DMSO) spectrum of M7, Related to Table 1.

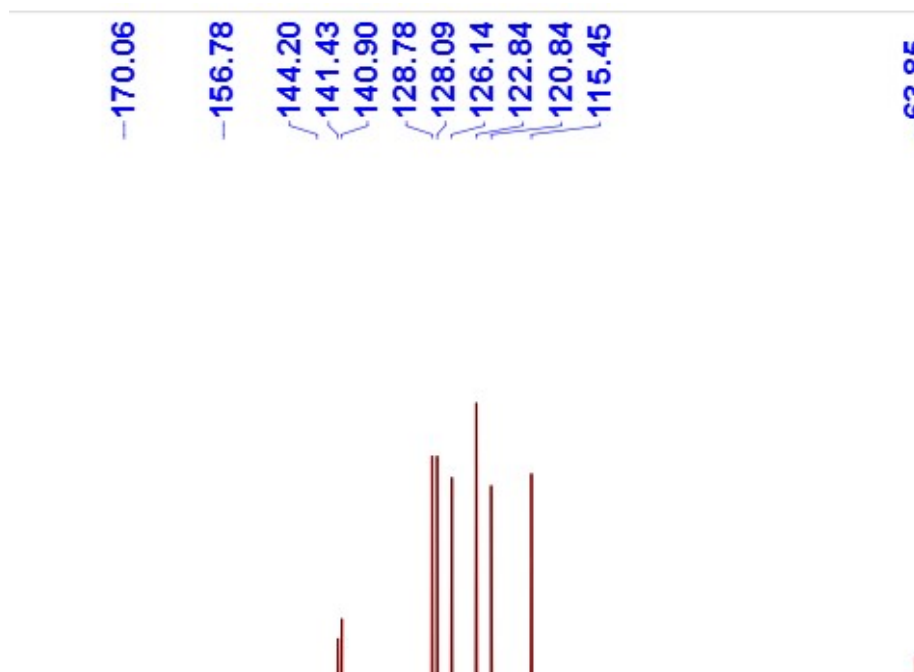


Figure S26 – The  $^{13}\text{C}$  NMR (500 MHz, DMSO) spectrum of M7, Related to Table 1.

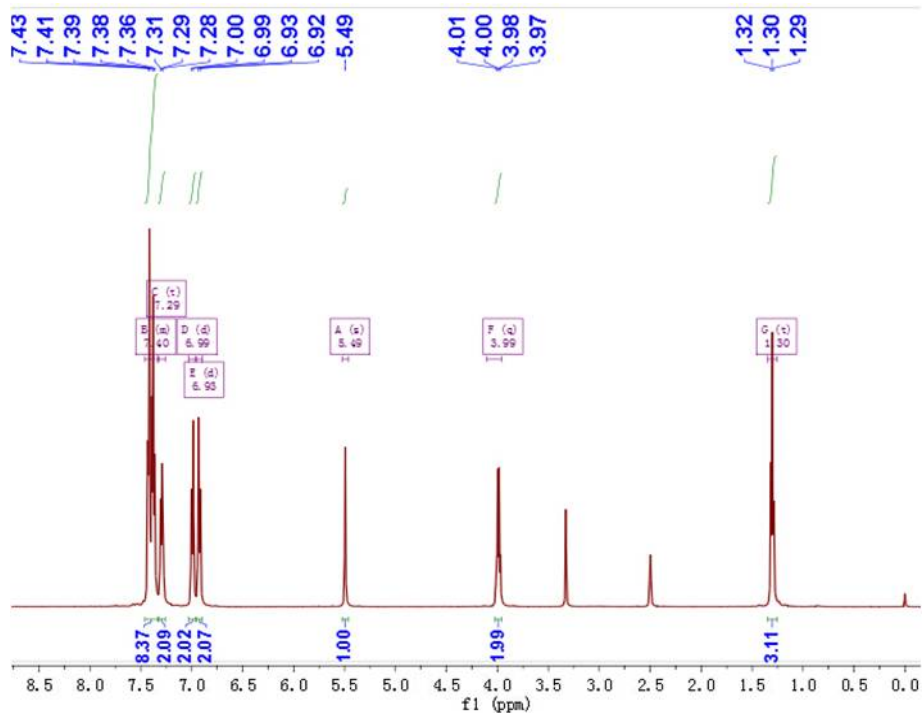


Figure S27 – The  $^1\text{H}$  NMR (500 MHz, DMSO) spectrum of M8, Related to Table 1.

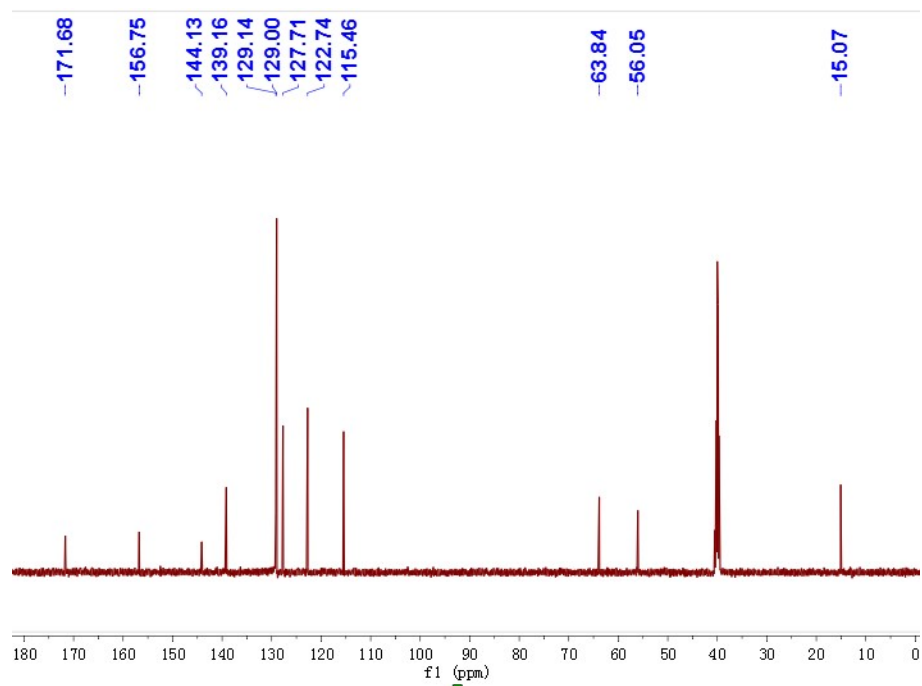


Figure S28 – The  $^{13}\text{C}$  NMR (500 MHz, DMSO) spectrum of M8, Related to Table 1.



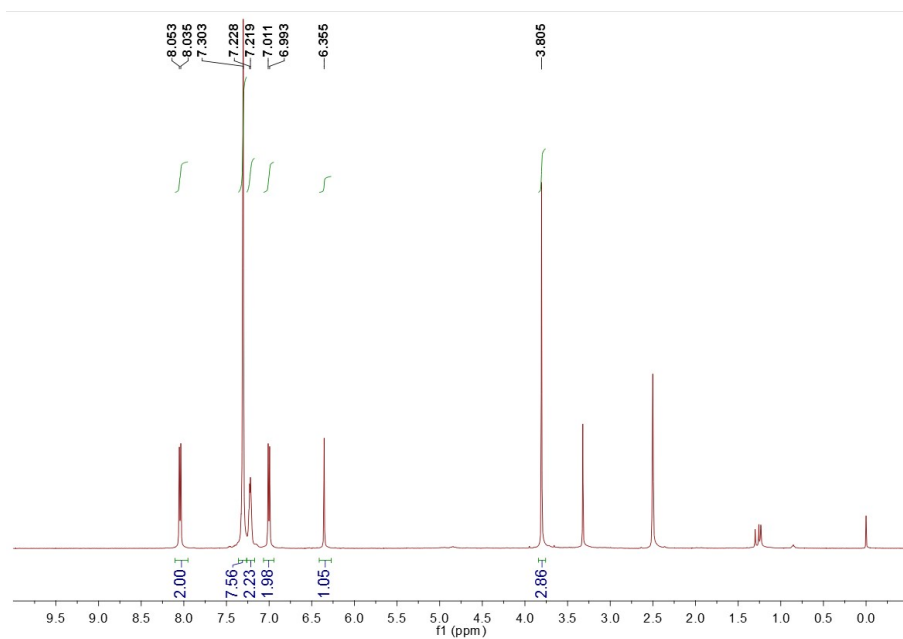


Figure S29 – The  $^1\text{H}$  NMR (500 MHz, DMSO) spectrum of M9, Related to Table 1.

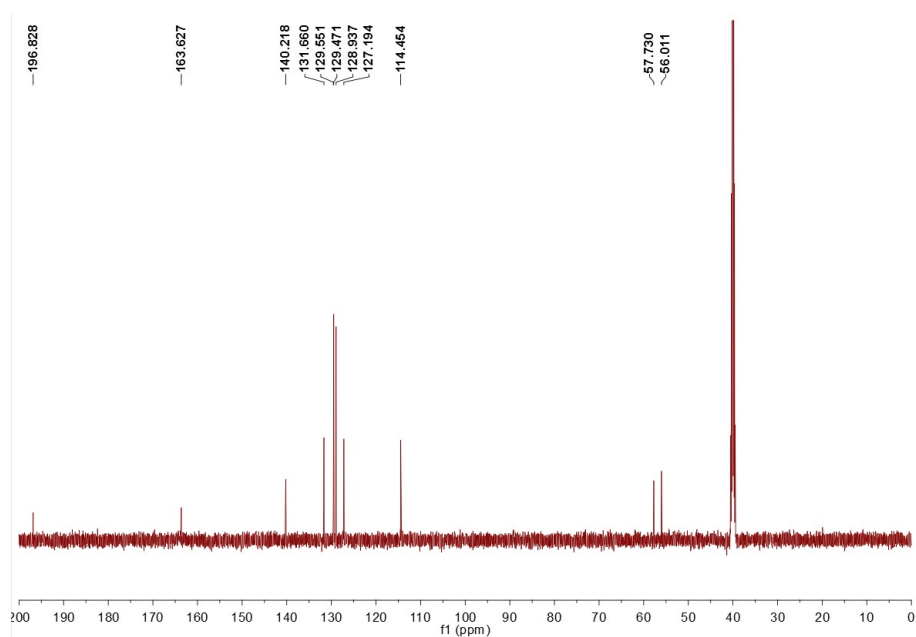


Figure S30 – The  $^{13}\text{C}$  NMR (500 MHz, DMSO) spectrum of M9, Related to Table 1.

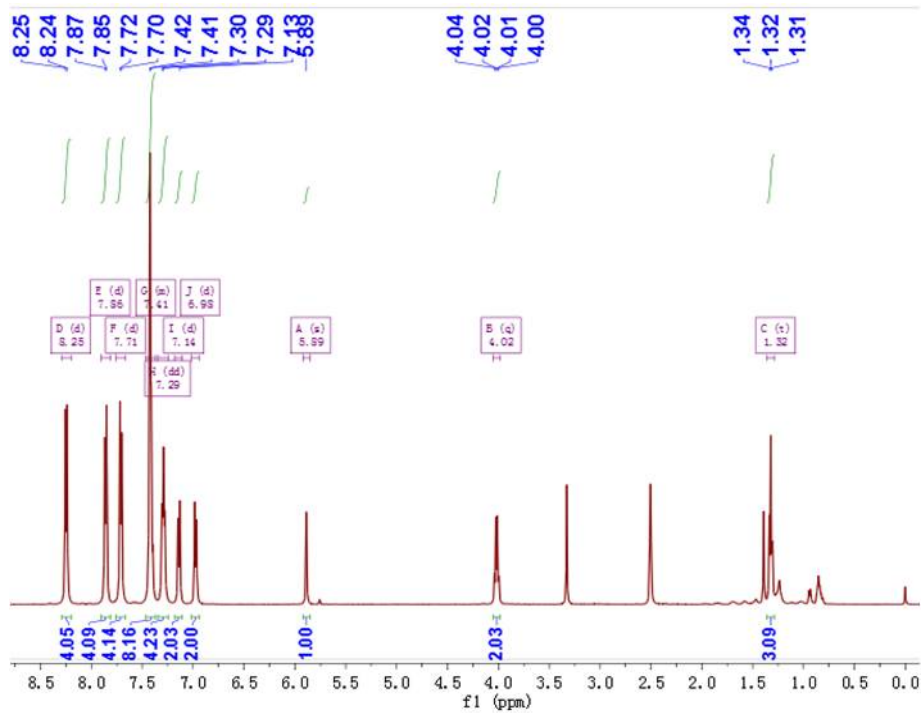


Figure S31 – The  $^1\text{H}$  NMR (500 MHz, DMSO) spectrum of M10, Related to Table 1.

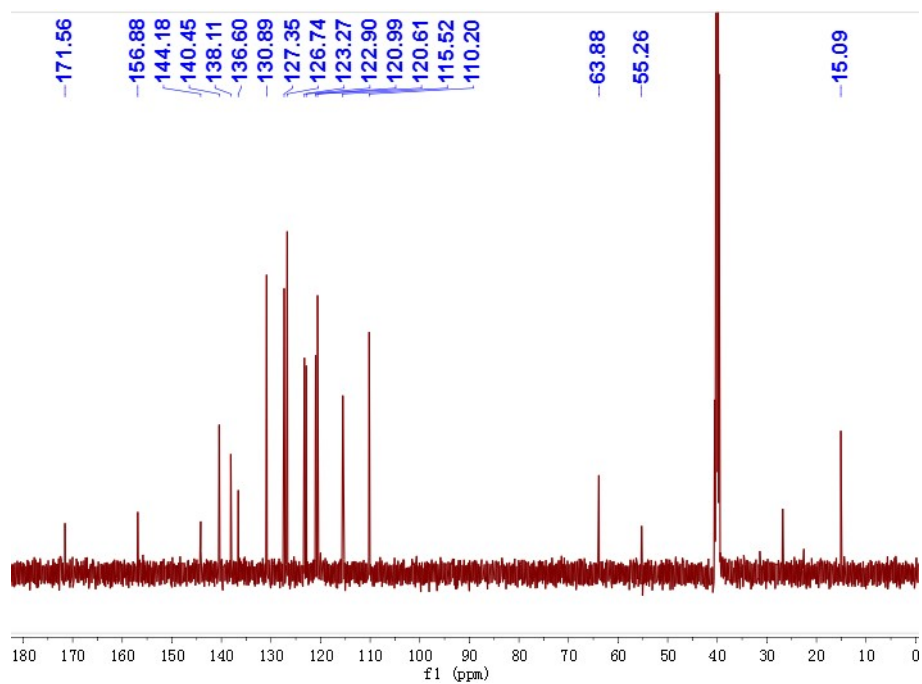
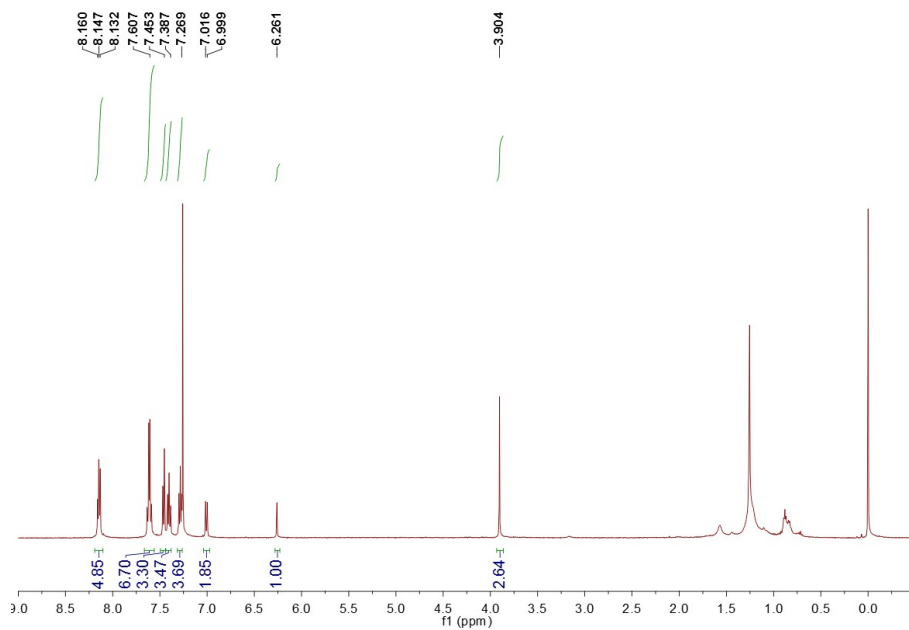
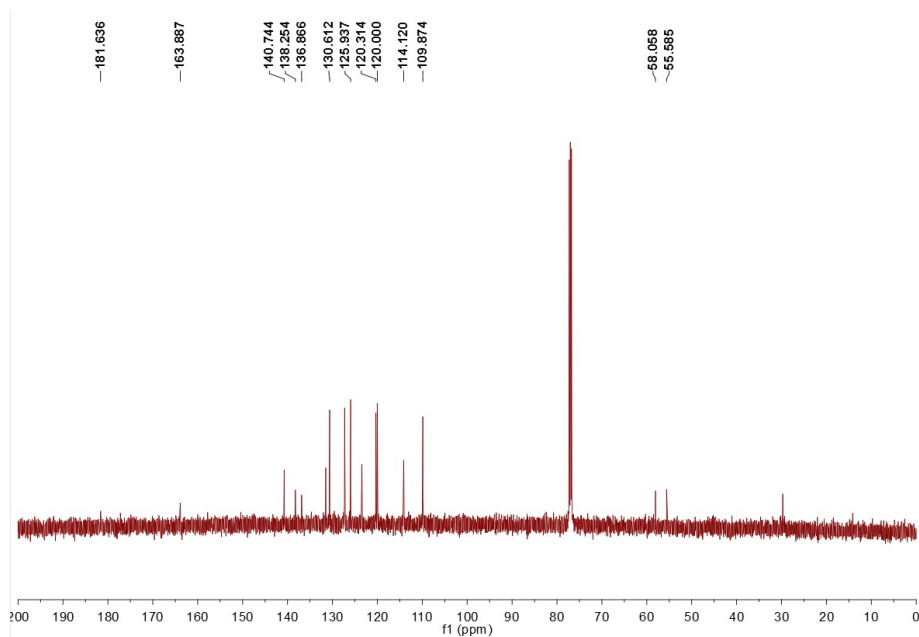


Figure S32 – The  $^{13}\text{C}$  NMR (500 MHz, DMSO) spectrum of M10, Related to Table 1.



**Figure S33 – The  $^1\text{H}$  NMR (500 MHz, DMSO) spectrum of M12, Related to Table 1.**



**Figure S34 – The  $^{13}\text{C}$  NMR (500 MHz, DMSO) spectrum of M12, Related to Table 1.**

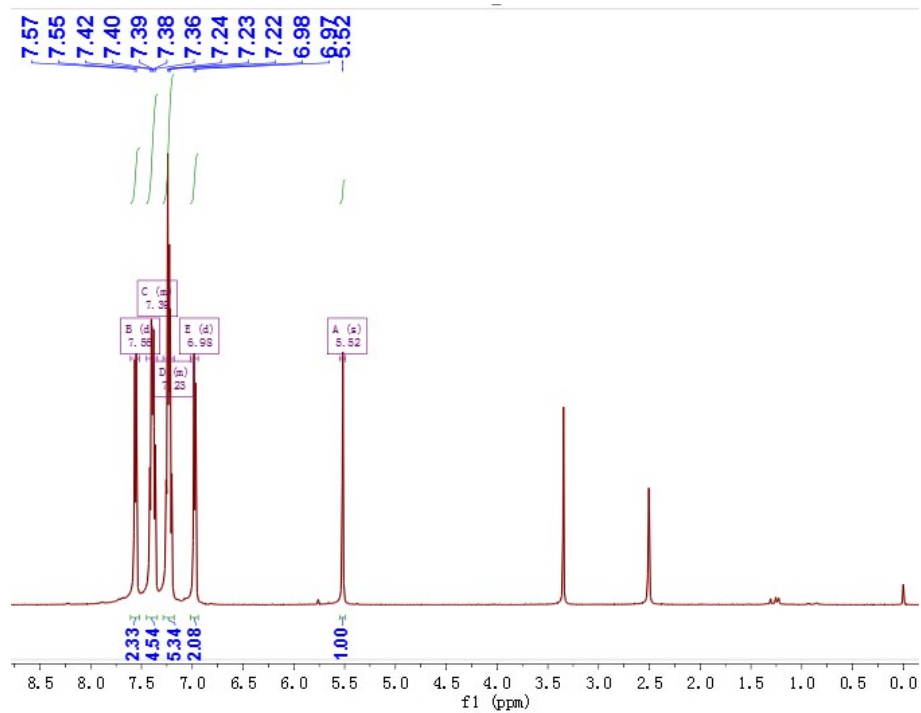


Figure S35 – The  $^1\text{H}$  NMR (500 MHz, DMSO) spectrum of M13, Related to Table 1.

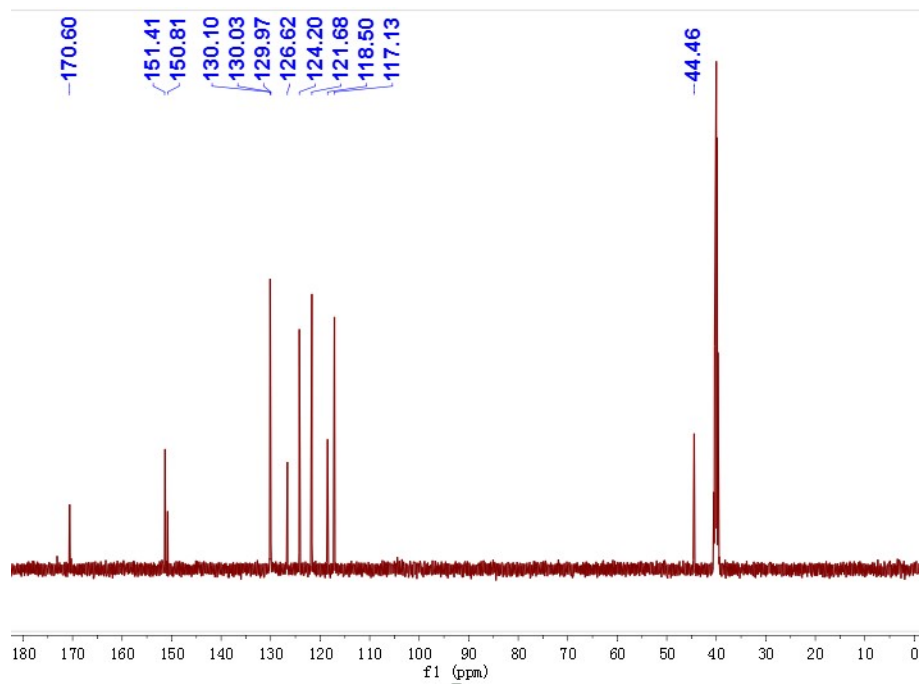


Figure S36 – The  $^{13}\text{C}$  NMR (500 MHz, DMSO) spectrum of M13, Related to Table 1.

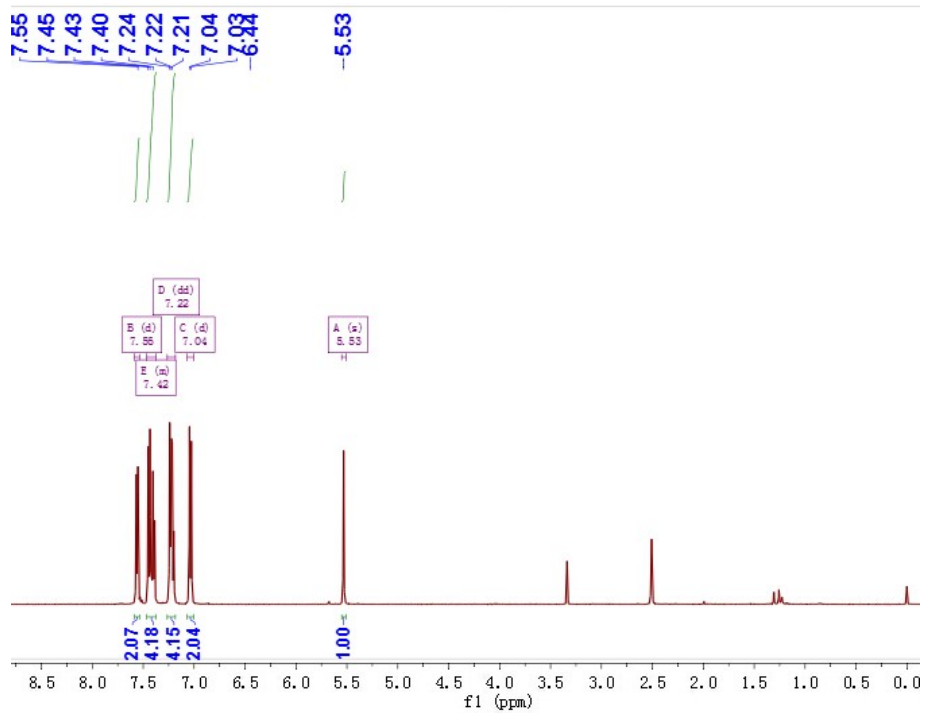


Figure S37 – The  $^1\text{H}$  NMR (500 MHz, DMSO) spectrum of M14, Related to Table 1.

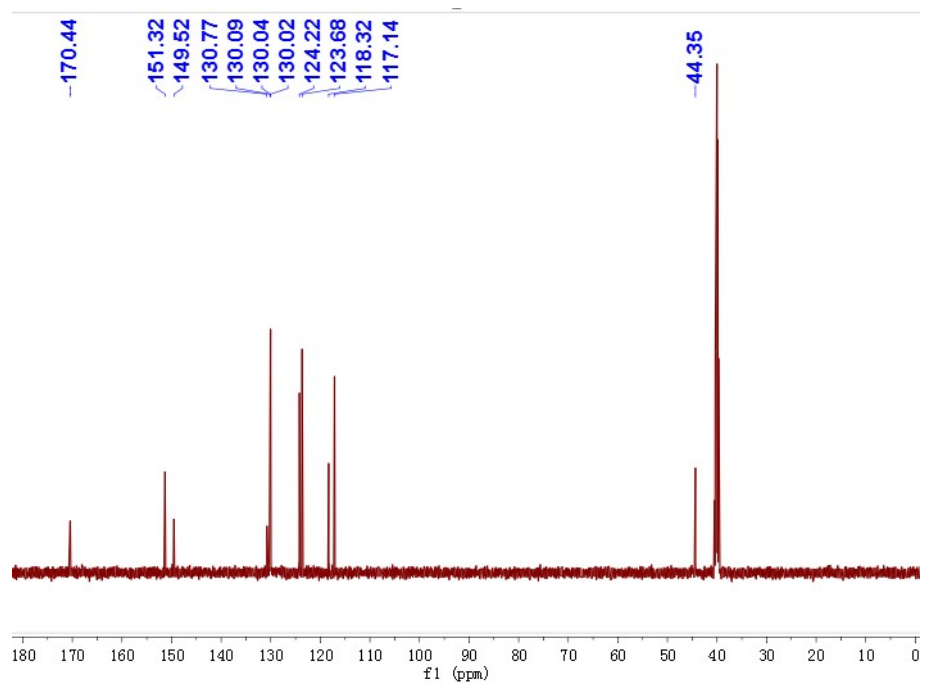


Figure S38 – The  $^{13}\text{C}$  NMR (500 MHz, DMSO) spectrum of M14, Related to Table 1.

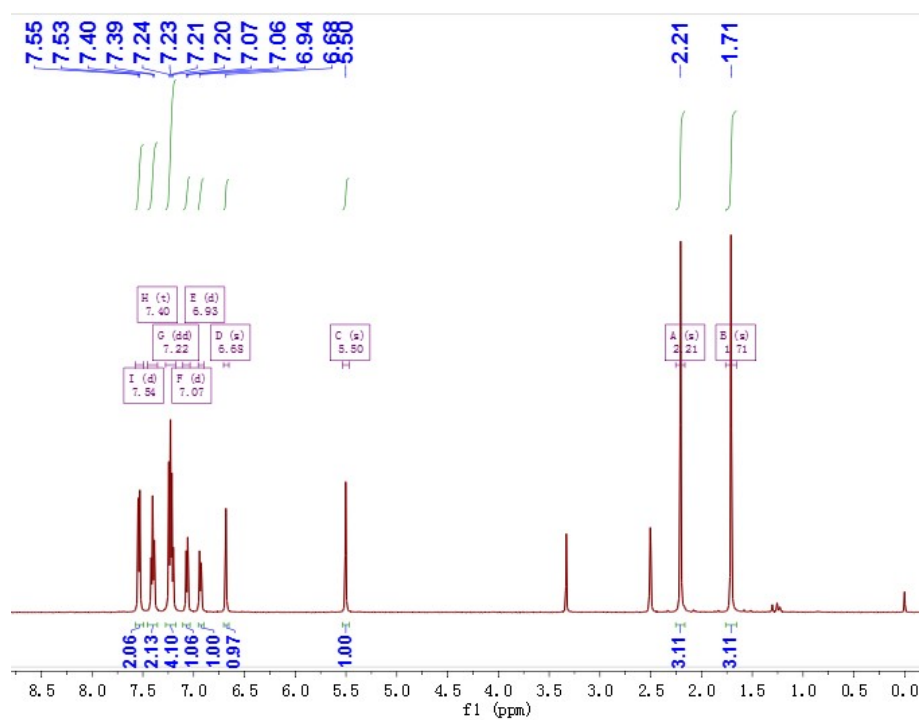


Figure S39 – The  $^1\text{H}$  NMR (500 MHz, DMSO) spectrum of M15, Related to Table 1.

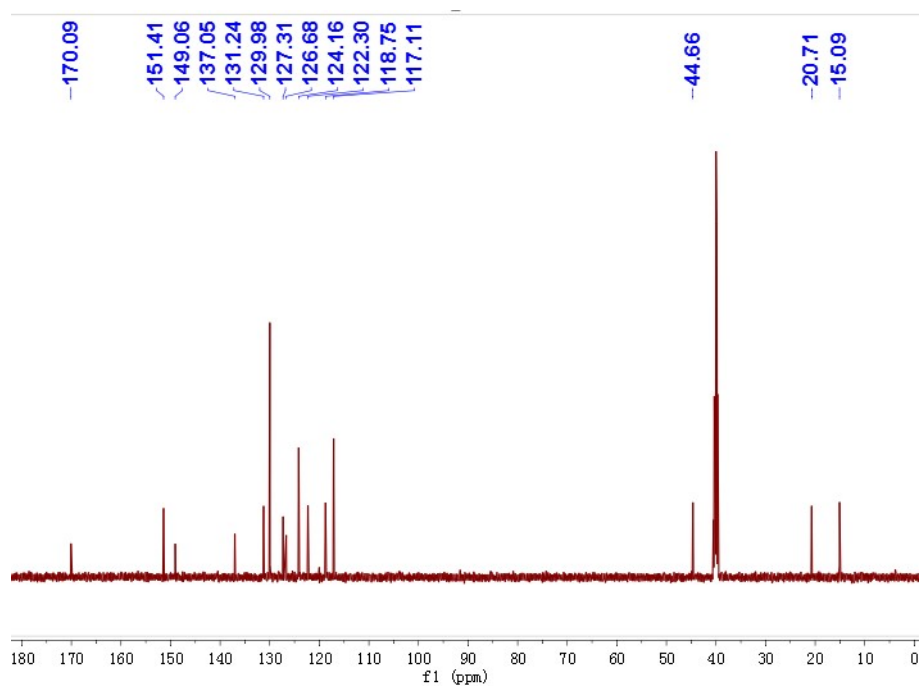


Figure S40 – The  $^{13}\text{C}$  NMR (500 MHz, DMSO) spectrum of M15, Related to Table 1.

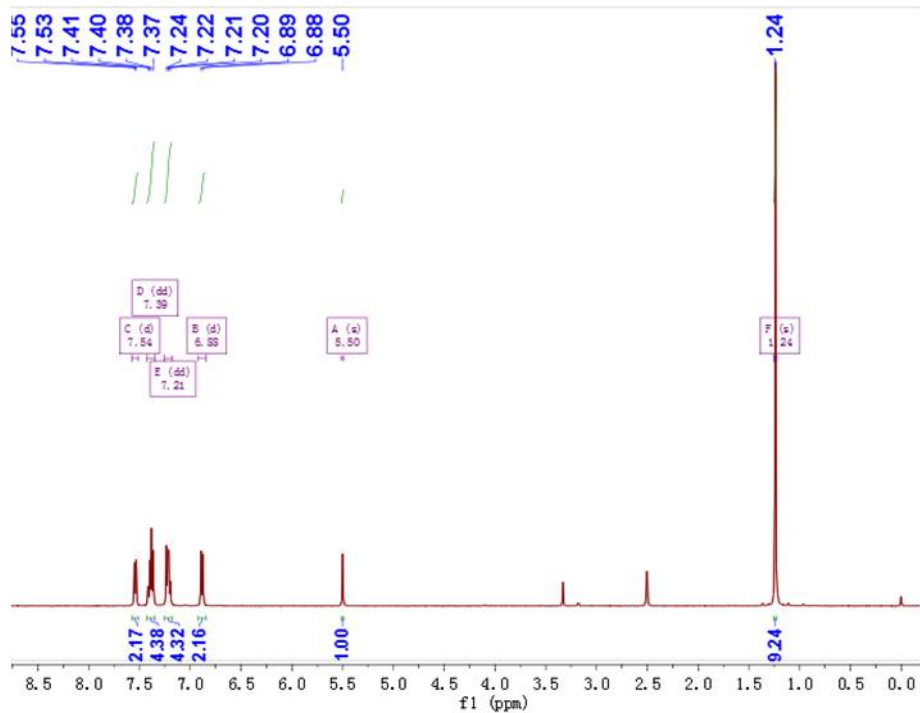


Figure S41 – The  $^1\text{H}$  NMR (500 MHz, DMSO) spectrum of M16, Related to Table 1.

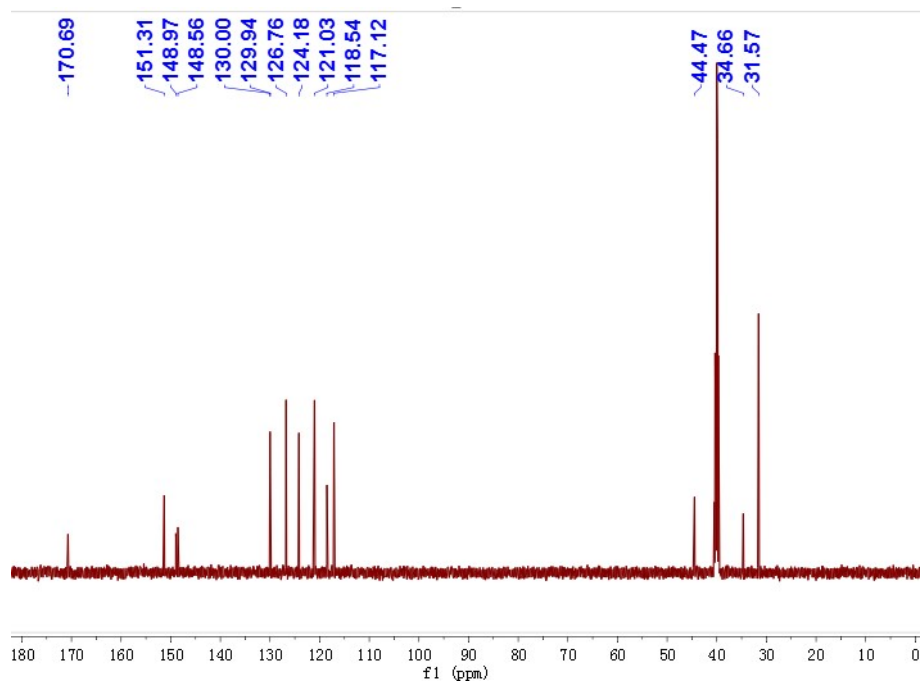


Figure S42 – The  $^{13}\text{C}$  NMR (500 MHz, DMSO) spectrum of M16, Related to Table 1.

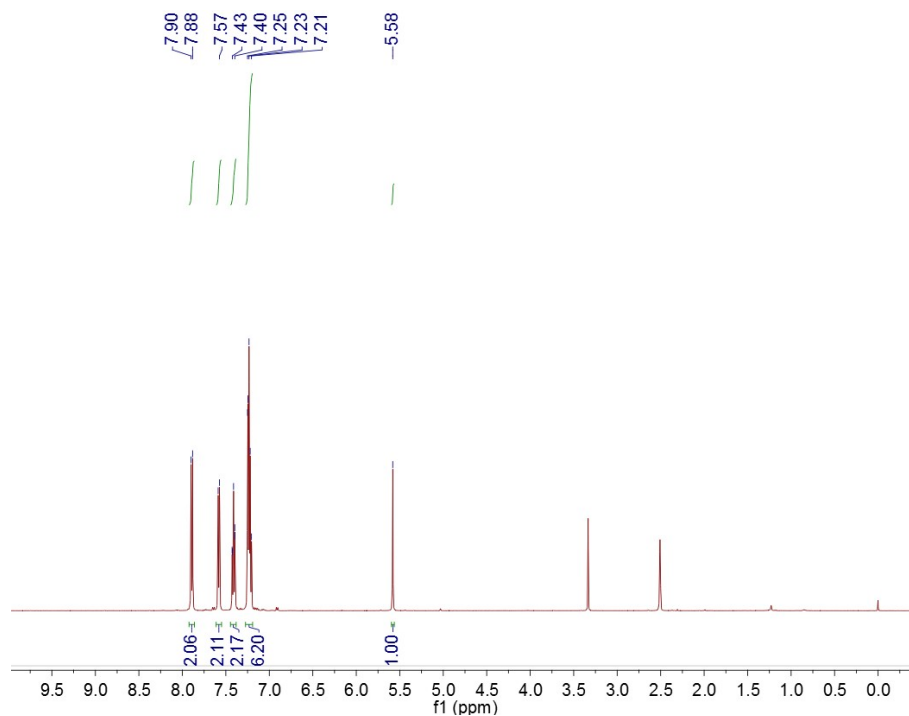


Figure S43 – The  $^1\text{H}$  NMR (500 MHz, DMSO) spectrum of M17, Related to Table 1.

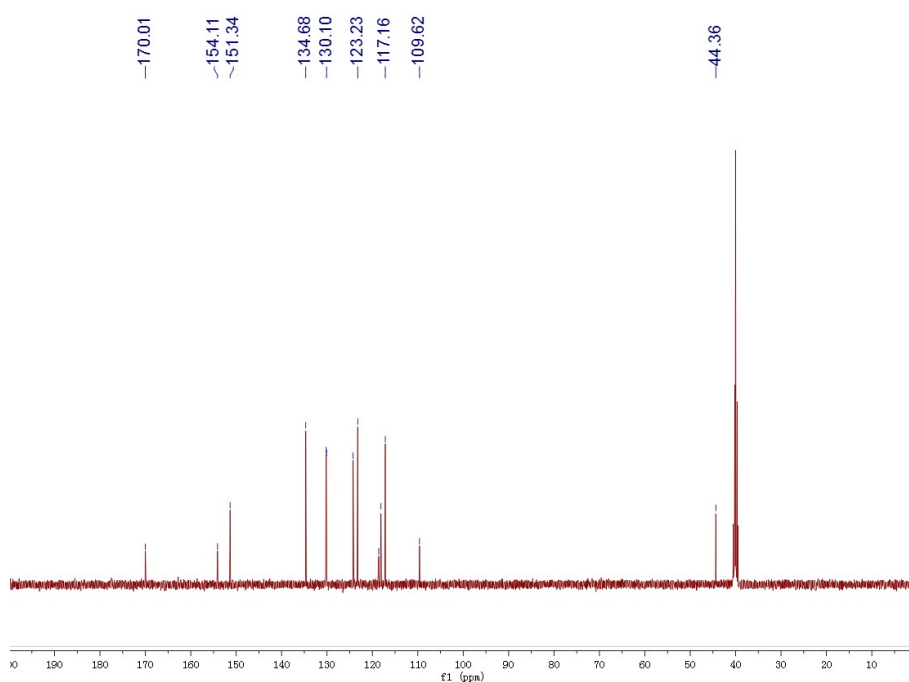


Figure S44 – The  $^{13}\text{C}$  NMR (500 MHz, DMSO) spectrum of M17, Related to Table 1.



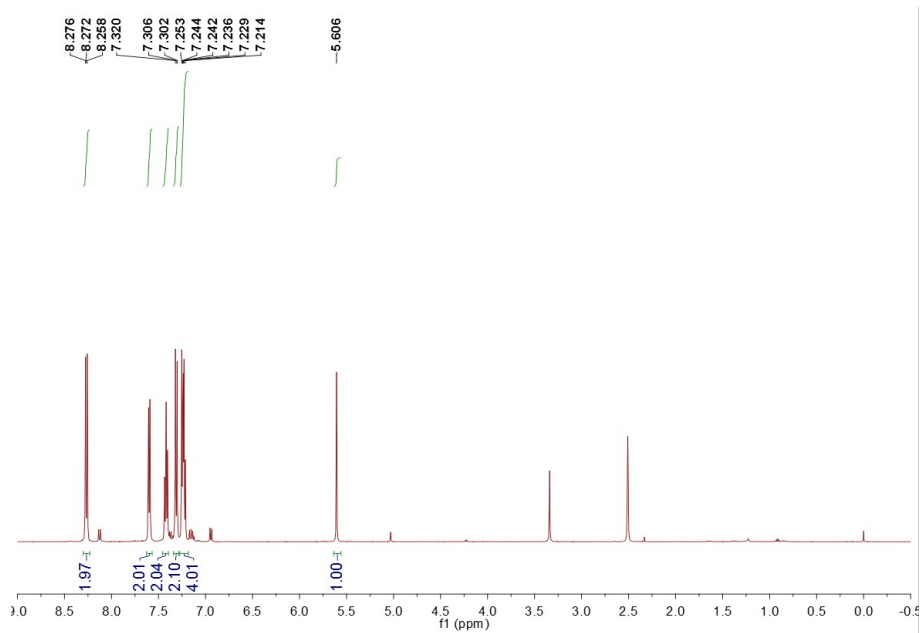


Figure S45 – The  $^1\text{H}$  NMR (500 MHz, DMSO) spectrum of M18, Related to Table 1.

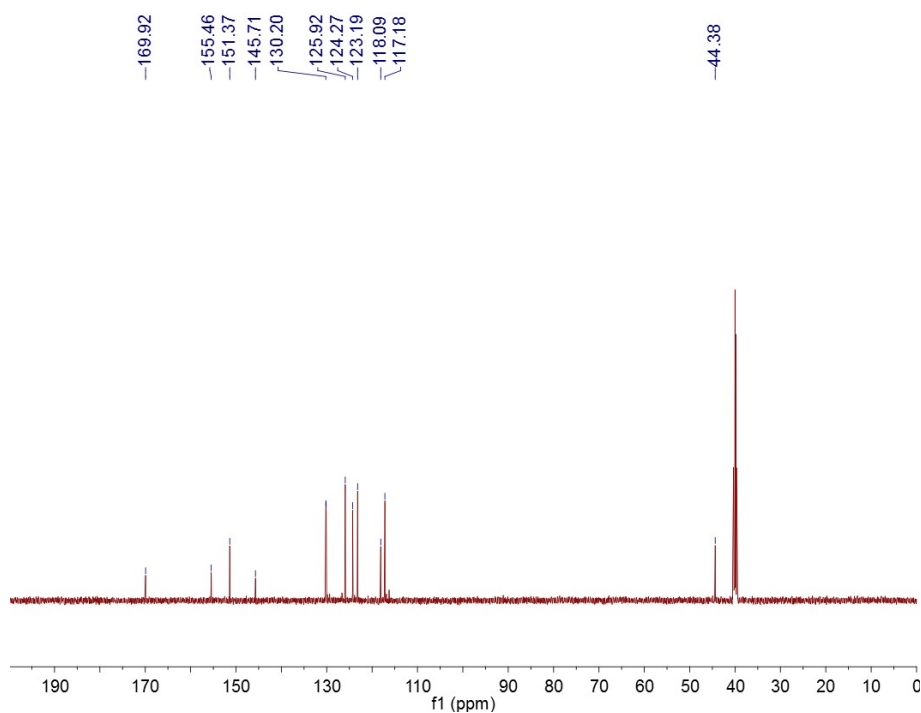


Figure S46 – The  $^{13}\text{C}$  NMR (500 MHz, DMSO) spectrum of M18, Related to Table 1.